Chapter 1

Studies of the Auger Observatory Fluorescence Telescope performance

The LIP group has developed a new simulation based on Geant4 where the complete geometry of the Auger fluorescence telescope is implemented. This new tool was used to study in detail the performance of the telescopes in terms of optical quality and efficiency. The results obtained were compared with the standard simulation and with laser events.

1.1   Auger Fluorescence Telescopes

The Auger Fluorescence Detector (FD) is composed of 24 Fluorescence Telescopes. The telescopes are disposed in four eyes overlooking the Surface Detector array. Each eye has a Field Of View (FOV) of $28.6° \times 180°$. Each of the 24 Fluorescence Telescopes is a modified Schmidt camera.

The Schmidt telescope design is based on the use of a spherical mirror with an aperture stop at the centre of curvature. This design produces uniform images in a spherical focal surface, with its centre of curvature coincident with the one of the mirror. A corrector plate in the aperture is introduced to correct the spherical aberration of the telescope. A more complete description of the Schmidt camera can be found in [1].

The scheme of the telescopes and a picture of one of them is shown in figure 1.1 where the filter, the corrector ring, the mirror and the camera are visible.
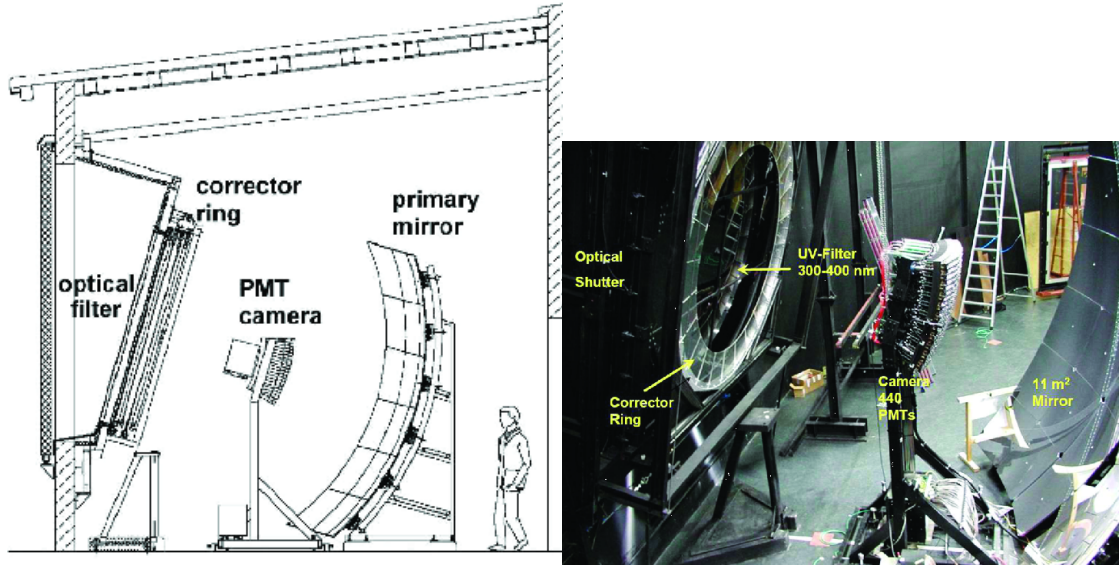
Figure 1.1: The Auger Fluorescence telescopes. Left: Scheme of the telescopes. Right: Photograph of a telescope with its main components indicated.

Filter

The first optical component of the Auger fluorescence telescopes is an UV filter. The filter is placed at the entrance pupil of the telescope. The main function of the filter is to select the interesting wavelength range at the entrance of the telescope. Besides its main function the filter also protects the telescope from exterior elements such as wind, dust, rain, etc.

The filter is a glass plate made of Schott M-UG6 glass. It is reinforced, mechanically, by a metallic grid. This filter presents a high transmittance in the UV-B region and high absorption in the visible and infra-red regions. The detailed characteristics of M-UG6 can be found in [2].

Corrector Ring

In telescopes with this design, a corrector plate is used to pre-correct the light rays, that will arrive to the mirror, in order to reduce the spherical aberration introduced by the use of a spherical mirror. The spherical aberration increases as the light rays enter far from the optical axis. The requirements of the Auger FD of having a spot size of 14/15 mm, that corresponds to an angular dimension of 0.5°, avoids the use of this plate for a radius smaller than 0.85 m. Since the aperture of the telescope has an outer radius of 1.1 m, a correction was still necessary. For simplicity a circular ring was introduced to correct light rays that enter with a radius $0.85 < R < 1.1$ m. This lens is called the "corrector ring".
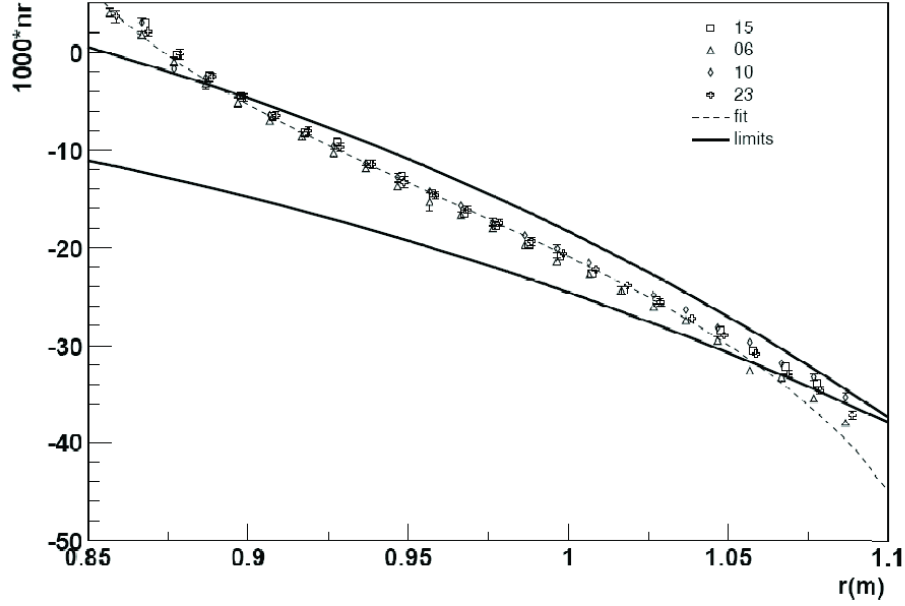
Figure 1.2: The corrector ring profile: radial component of the normal to the lens curved surface as a function of the radius. Solid lines represent the bounds used for quality control. The different markers represents the measurements performed in different samples.

The corrector ring is basically a lens with one flat side. A sixth order polynomial is used to describe the curved surface of the corrector ring. This design allows the spherical aberration to be corrected and the production of a spot within the requirements for the Auger FD. However such curvature is difficult to realise with the necessary optical quality. The profile of the lens has been optimised taking into account the production process and the fact that only a ring is used in the telescope. More details on the production of the corrector ring can be found in [3, 4]. The production process could not perfectly assure the form of the lens profile. However, the limits for the radial inclination of the surface were defined and used for quality control. Figure 1.2 shows the bounds for the radial component of the normal to the surface as well as measured profiles for different samples. It can be seen that the measured profile respects the bounds, except in the limit regions, i.e in the outer part of the ring where it goes above the bound and in the inner part where it goes below the bound. The corrector ring profile will be discussed in detail below in this chapter.

Mirror

The modified Schmidt camera of the Auger fluorescence telescope uses a spherical mirror. This mirror has a radius of curvature of $R = 3.4$ m. It has a square format and measures $3.6\,\text{m} \times 3.6\,\text{m}$ having a collection area of about $13\,\text{m}^2$. Due to the large area the mirrors were built as an array of segments. Two eyes are equipped with mirrors built in Germany, which are made up by an array of rectangular mirrors. The other two eyes have installed mirrors from the Czech Republic which are made of an array of hexagonal-shaped mirrors.

Camera

The focal surface of the fluorescence telescopes is defined as a spherical surface concentric with the mirror surface. The focal surface has a radius of 1.743 m, corresponding to the surface where the disc of least confusion is located for the different incident angles.

The fluorescence light from an EAS is focused onto the focal surface where a PMT camera [5] is installed. The camera, which can be seen in figure 1.1, is composed by 440 hexagonal pixels distributed in an array with 22 rows and 20 columns. The pixel has a side-to-side distance of 45.6 mm that corresponds to an angular distance of 1.5°. The pixels are spaced in equal steps of azimuthal angle and equal steps of elevation angle. The FOV of the telescope is of 30° in azimuth and of 28.6° in elevation. The smaller FOV in elevation, even with a higher number of rows than columns, is due to the stacking of the hexagonal pixels to produce a continuous focal surface

The PMTs used for the Auger fluorescence telescopes have an hexagonal shape. A gap between adjacent PMTs is needed for mechanical reasons. In addition, the PMTs are quite inefficient near the borders. To overcome these problems, light guides were introduced. The light guides define a pixel in the ideal focal surface and direct the light, that would otherwise be lost, to the active region of the PMTs, where it can be detected.

The light guide is realised with six reflecting pieces called Mercedes. A scheme of the light guide and a photograph of a detail of the camera with Mercedes stars are shown in figure 1.3. Each Mercedes is a star with three arms separated by 120°. The cross section of each arm is an isosceles triangle with a base of 9.2 mm and a height of 18 mm. The top of six Mercedes define a pixel in the ideal focal surface.

The PMTs are place behind the light guides. The PMT used is a XP3062 from Photonis. The XP3062 is an 8-stage PMT with a hexagonal window and a standard
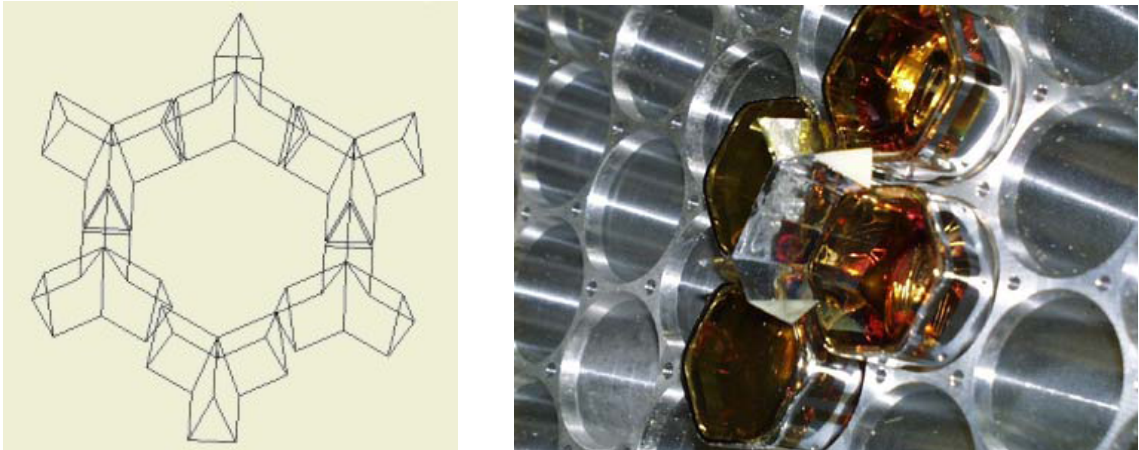
Figure 1.3: The Light Guides of the Auger Camera. Left: Scheme of six Mercedes that are joined to form a pixel light guide. Right: Photograph of a detail of the camera with four PMTs and two Mercedes stars installed.

bi-alkaline photocathode. Its quantum efficiency is evaluated as 25% for wavelengths of $250-400\,\text{nm}$. The nominal gain for FD operation is set at 5×10^4. The electronics of the fluorescence telescope samples the signal collected by the PMTs each $100\,\text{ns}$.

The camera body is approximately of square shape, measuring 93 cm in the horizontal dimension and 86 cm in the vertical one. The camera is held in place using a simple support of two legs. The legs of the camera are made of C-shaped steel 5 cm wide. The camera, including its body, electronics and support structure will produce an obscuration in the telescope mirror, reducing the light collection area.

1.2   Simulation of the Telescopes

1.2.1   The simulation framework

The Pierre Auger Observatory has developed a general framework for the simulation of the detector and for data reconstruction and analysis - the $\overline{\text{Off}}\ \underline{\text{line}}$ [6].

This framework was mainly developed using the C++ programming language and several toolkits and external libraries like ROOT, Geant4, BOOST, Xerces, etc. The $\overline{\text{Off}}\ \underline{\text{line}}$ is a modular software, each module performing a specific simulation or reconstruction task. XML files are used to configure the software. Each module used has an associated XML file where the module parameters are configured. The sequence of modules to be run is also configured with a XML file. Data are exchanged between the different modules through the use of a C++ class that contains the event

data.

The simulation of a fluorescence event consists of several steps required to estimate the signal recorded by each telescope when a shower develops in its FOV. First the longitudinal profile of the shower is generated. Then the amount of light arriving at the telescope pupil is estimated. To do this the production of the fluorescence light is simulated as well as the propagation and attenuation of this light in the atmosphere. Currently the fluorescence light arriving at the telescope pupil is described in the following way. The arrival times are binned with a time constant of 10 ns, which is ten times lower than the time sampling of the telescope electronics, and arrays with the number of photons and the viewed direction in each time bin are filled. Using this information, photons are then generated at random positions in the diaphragm of the telescope. For each time bin, photons are given the direction of the bin, a random position in the diaphragm and a weight. The sum of the weights of all generated photons corresponds to the total number of photons for that direction. The simulation of the telescope will then propagate these photons in the telescope and record the signal (in photons) registered in the focal surface. Noise is then added and the electronics and the trigger system are simulated. These tasks constitute the core of the simulation and are performed by different modules. Other modules execute more general tasks like the generation of the event structure and the output of the result in several formats. Several modules can be chosen alternatively to execute a specific task simply by changing the module sequence configuration file. For example the shower longitudinal profile can be generated by a module that uses a parametrisation or by a module that reads data from an external simulation program. This module, in turn, can be configured to read data from AIRES, CORSIKA or CONEX. The simulation of the fluorescence telescope can now be performed using one of two modules: the TelescopeSimulatorKG or the TelescopeSimulatorLX, the new simulation developed at Lisboa using the Geant4 toolkit.

1.2.2   The TelescopeSimulatorKG

The TelescopeSimulatorKG is a custom ray-tracing module developed by the Karlsruhe Auger Group. Currently this module is used as the standard telescope simulation module in the $\overline{\text{Off}}$ line. A photon entering the diaphragm is passed, sequentially, by the several optical elements, always in the same order. This fact makes it possible to develop a simple custom ray-tracing code that simulates, in sequence, the several optical elements of the telescope.

A photon enters the telescope diaphragm with a certain direction, position and weight. This weight, w, allows one simulated photon to represent w photons that are propagated like a bunch. Such a photon is passed from the PhotonGenerator module to the TelescopeSimulator module. Then the interaction with the filter is simulated. The position and direction of the photon is maintained but its weight is multiplied by the filter transmittance. Next the corrector ring is simulated. If the position of the photon has a radius, relative to the optical axis, greater than the inner radius of the corrector ring the photon suffers two refractions in the two surfaces of the corrector ring. First the photon is refracted in the curved surface of the corrector ring. Then the position of the photon in the flat surface is calculated with the direction of the photon after the first refraction. Finally the photon suffers the second refraction in the flat surface. The weight of the photon is once again altered by taking into account the transmittance of the corrector ring. Thus, the corrector ring changes the position, direction and weight of the photon. Afterwards the position at which the photon will hit the mirror is calculated. In this step it is verified whether the photon will hit the back of the camera, and thus be killed, as well as whether the photon will pass outside the mirror area. If the photon hits the mirror, it is reflected taking into account the mirror reflectivity in the photon weight. Next the position of the photon in the camera is calculated. If the photon hits a light guide, one or more reflections are simulated until the photon hits a PMT. The reflectivity of the light guides is taken into account at each reflection. The fact that the photon can be reflected in the PMT window before hitting the photocathode of the PMT is taken into account. The quantum efficiency of the PMT is also introduced in the photon weight. When a photon hits a PMT photocathode it is added to the signal of that PMT with a weight (representing the number of detected photons) that reflects the input weight (which represents the number of photons at the diaphragm) multiplied by the efficiencies of the several optical elements of the telescope.

The simulation is performed for a normalised wavelength of $\lambda_{\mathrm{norm}} = 370\,\mathrm{nm}$. The different photon wavelengths are taken into account by introducing a relative efficiency by which the output weight is multiplied.

1.2.3   The TelescopeSimulatorLX

Overview

The TelescopeSimulatorLX is an $\overline{\mathrm{Off}}\ \underline{\mathrm{line}}$ module for the simulation of the Auger fluorescence telescopes using the Geant4 toolkit [7, 8]. This module was developed

1 in Lisboa with the aim of performing a cross-check with the standard simulation and
2 of performing detailed studies of the fluorescence telescopes. Three persons from
3 LIP (Patrícia Gonçalves, Bernardo Tomé and me) were involved in the development
4 of this code representing a total effort of about 2 FTE (Full Time Equivalent).
5 Patrícia and Bernardo were responsible for the implementation of the geometry and
6 processes in the Geant4 framework while I was responsible for its integration in the
7 $\overline{\text{Off}}$ $\underline{\text{line}}$ framework and the development of the analysis tools. To allow for direct
8 comparisons with the previous code, the TelescopeSimulatorLX was integrated inside
9 the TelescopeSimulatorKG that had to be altered to record the properties of photons
10 at the different locations.

11   Geant4 is a software toolkit developed in the C++ programming language. It
12 simulates the passage of particles through matter. The user defines the geometry
13 and composition of the media, as well as a primary particle and its properties, and
14 then passes the control of the simulation to the kernel of Geant4. The kernel will
15 then take care of the tracking and interactions of the primary and secondary particles
16 throughout the defined "world", taking into account the properties of the traversed
17 materials. Whenever a particle (a photon in the present application) interacts with
18 a "sensitive detector", the relevant information is saved. The kernel will return when
19 there are no more particles to be tracked. Besides the actual sensitive detectors
20 existing in each detection system (the PMTs in the present case), virtual sensitive
21 detectors can be introduced in any part of the system in order to save the particle
22 information. This feature is used for testing purposes throughout this chapter.

23   The TelescopeSimulatorLX module was developed taking advantage of the capa-
24 bility to define arbitrarily complex geometries in Geant4 and of its ability to track
25 optical photons and simulate the various optical processes. In the TelescopeSimula-
26 torLX the geometry of the Auger fluorescence telescopes is implemented with their
27 detailed optical properties. The implementation of the several components will be
28 discussed in the following paragraphs.

29   For each photon generated by the PhotonGenerator module of the $\overline{\text{Off}}$ $\underline{\text{line}}$ a
30 primary optical photon, with the same characteristics (position, direction and wave-
31 length) is defined in Geant4. At this point the Geant4 kernel takes control of the
32 simulation of that photon in the telescope. The photon interacts with the several
33 pieces of the telescope. In this process the characteristics of the photon are changed
34 and the photon can even be killed. The photons are killed with a probability that
35 reflects the several inefficiencies of the optical system. Several sensitive detectors are
36 implemented so that detailed studies of the different components of the telescope
37 can be performed. The properties of the photons that hit these sensitive detec-

1 tors are recorded in a separate ROOT file for analysis. The PMTs are simulated
2 using sensitive detectors. When a photon hits one of these detectors the signal is
3 added to the PMT trace, the photon is killed and Geant4 returns the control to the
4 TelescopeSimulatorLX that will call Geant4 with the next photon.

5   The implementation of the telescope geometry and material definition was the
6 key task in the development of the simulation using the Geant4 toolkit. For each
7 optical component of the telescope a solid in space with the correct geometry must
8 be defined, as well as the optical properties of the component material. The main
9 challenges in this work were the detailed definition of a relatively complex geometry,
10 and the use of Geant4 for optical applications, which is not very common.

Filter

12 The filter of the Auger fluorescence telescopes is implemented as a disk made of
13 M-UG6. The disk has a diameter of 2.2 m and a thickness of 3.25 mm. The filter
14 is positioned perpendicular to the optical axis of the telescope, 10 cm before the
15 corrector lens geometric centre. Its centre coincides with the optical axis. The opti-
16 cal properties (refractive index and transmittance) are described in the simulation
17 following the manufacturer datasheet [2] for this type of material. The refractive in-
18 dex is described in the simulation as 1.526, independent of the photons wavelength.
19 The bulk absorption in the material is implemented as a tabulated function of the
20 absorption length versus the photons wavelength. The absorption length is calcu-
21 lated from the transmittance that assumes a nominal value of 0.83 at a wavelength
22 of 370 nm for a thickness of 3.25 mm.

Corrector Ring

24 The corrector ring is a fundamental piece of the telescope. It influences directly the
25 quality of the optical image produced. The lens is implemented using the Geant4
26 class G4Polycone. This class allows the implementation of a revolution solid by
27 defining the section of the solid and the angular limits for the revolution. The section
28 is defined through a series of points (r, z) that are joined by straight lines. Figure 1.4
29 shows three visualisations of the corrector ring. In the figures the curvature of the
30 corrector ring is exaggerated to be visible in the picture. The figure on the left shows
31 a revolution of $^3/_2\pi$. The figure on the centre is a magnification of the left one. The
32 figure on the right shows a corrector ring segment in which the profile of the curved
33 surface was described using only four points, to make visible the discretisation of
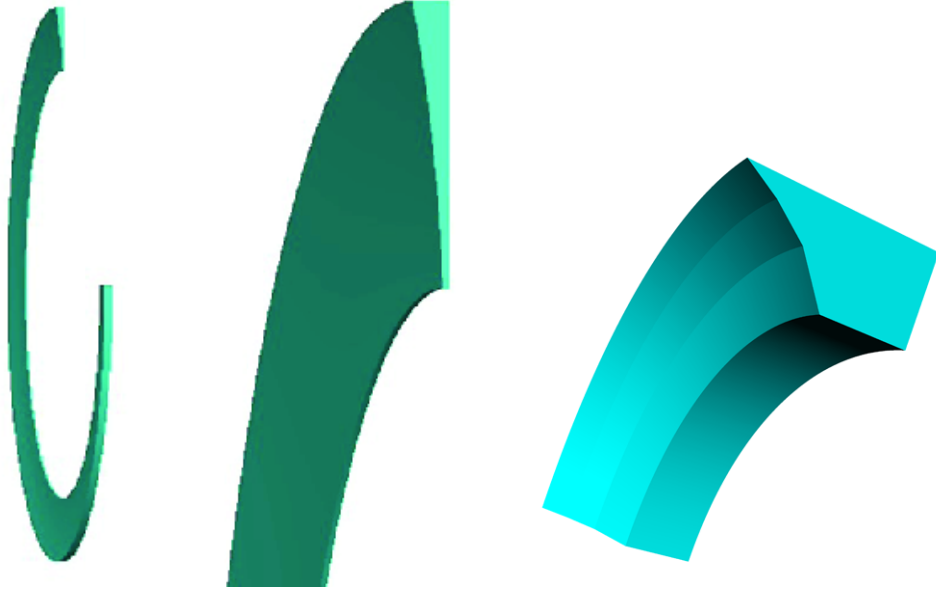34 the curved surface. The corrector lens profile can be characterised by the radial

Figure 1.4: The Auger FD corrector ring.

1 component of the normal to the curved surface, n_r, since the other component
2 can be obtained from the normalisation condition. In the TelescopeSimulatorLX
3 four corrector lenses with different profiles are implemented. The first one called
4 "KG" corresponds to the profile implemented in the TelescopeSimulatorKG and to
5 the theoretical profile described in [4]. The radial component of the normal as a
6 function of the radius is described by

$$n_{r_\text{KG}}(r) = \frac{4}{32\,(n-1)\,f^3} \cdot r^3 - \frac{3R_d^2}{32\,(n-1)\,f^3} \cdot r^3$$

7 where $n = 1.5$, $f = 1.657\,\text{m}$ and $R_d = 0.85\,\text{m}$. The second one is called the "circular"
8 profile and corresponds to a profile cut with a circular disk of radius R displaced
9 from the centre by y. This profile is described by

$$n_{r_\text{Circ}}(r) = \frac{r-y}{\sqrt{R^2 - (r-y)^2}}$$

10 where $R = 8.383\,\text{m}$ and $y = 0.79527\,\text{m}$. The third and fourth corrector lens profiles
11 implemented in the code correspond to the upper and lower limit for n_r in the
12 figure 1.2. The upper and lower limit curves in the figure were fit with third order
13 polynomial functions,

$$n_r(r) = a_1 \cdot r + a_2 \cdot r^2 + a_3 \cdot r^3$$

1 yielding, for the upper limit curve, $a_1 = 5.906 \times 10^{-3}$ m^{-1}, $a_2 = 94.52 \times 10^{-3}$ m^{-2},

2 $a_3 = -118.8 \times 10^{-3}$ m^{-3} and $a_1 = -22.25 \times 10^{-3}$ m^{-1}, $a_2 = 85.2 \times 10^{-3}$ m^{-2},

3 $a_3 = -87.52 \times 10^{-3}$ m^{-3} for the lower limit profile curve. These four profiles are

4 represented in figure 1.5(a) versus the radius of the lens. The corrector ring is

5 implemented in Geant4 by defining its physical dimensions, in particular the height

6 z. Figure 1.6 illustrates the geometry of the lens surface and the relation between

7 the normal vector and the height. The height of the curved surface can be defined

8 from $n_r(r)$ by:

$$z(r) = \int_{r_0}^{r} \frac{n_r(r')}{\sqrt{1 - n_r^2}} dr' \sim \int_{r_0}^{r} n_r(r') \, dr'$$

9 The four profiles then take the form:

$$z_{\text{KG}}(r) = z_0 + \frac{1}{32(n-1)f^3} \cdot r^4 - \frac{3/2 \cdot R_d^2}{32(n-1)f^3} \cdot r^2$$

$$z_{\text{Circ}}(r) = z_0 - \sqrt{R^2 - (r-y)^2}$$

$$z_{\text{Low}}(r) = z_0 + \frac{a_1}{2} \cdot r^2 + \frac{a_2}{3} \cdot r^3 + \frac{a_3}{4} \cdot r^4$$

$$z_{\text{Up}}(r) = z_0 + \frac{a_1}{2} \cdot r^2 + \frac{a_2}{3} \cdot r^3 + \frac{a_3}{4} \cdot r^4$$

10 or, numerically,

$$z_{\text{KG}}(r) = 0.00358557 + 0.0137377 \cdot r^4 - 0.0148882 \cdot r^2$$

$$z_{\text{Circ}}(r) = 8.38282 - \sqrt{70.2747 - (r - 0.79527)^2}$$

$$z_{\text{Low}}(r) = -0.00201816 + 0.011125 \cdot r^2 - 0.0284 \cdot r^3 + 0.02188 \cdot r^4$$

$$z_{\text{Up}}(r) = 0.00597899 - 0.002953 \cdot r^2 - 0.0315067 \cdot r^3 + 0.0297 \cdot r^4$$
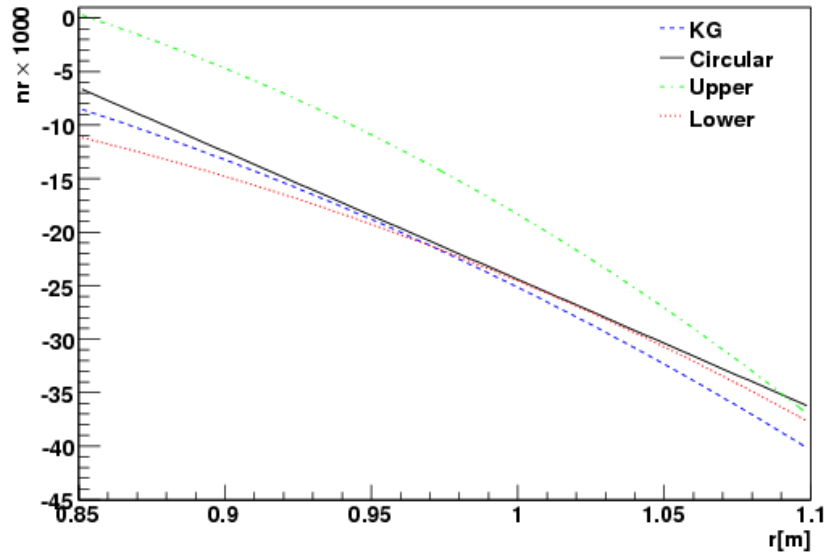
(a) Radial component of the normal to the curved surface of the corrector ring versus (n_r) the radius of the lens.
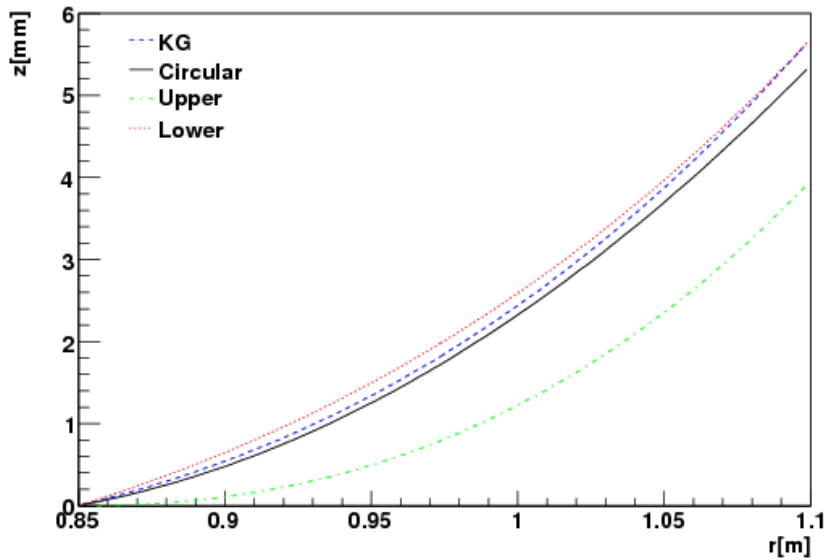
(b) Height of the curved surface of the corrector ring (z) versus the radius.

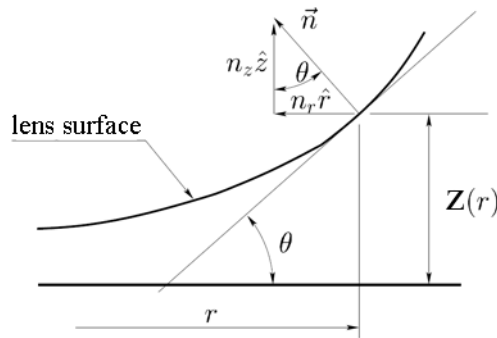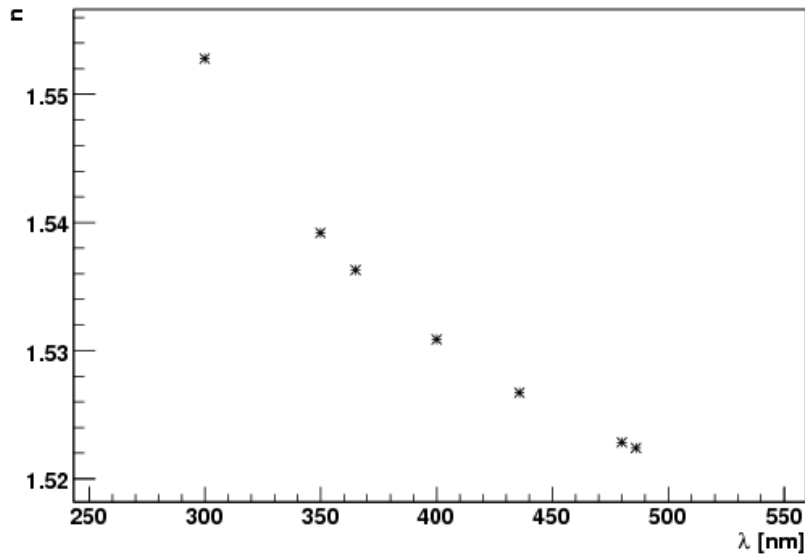Figure 1.5: The profiles of the corrector ring

Figure 1.6: Relation between the lens height $z(r)$ and its normal vector $\vec{n}$. r is the distance to the centre and n_r and n_z are, respectively, the radial and vertical components of the normal. Figure adapted from [4].

where the integration constant z_0 is used to set all profiles to zero at the radius $r = 0.85$ m. These four profiles are represented in figure 1.5(b). In the Geant4 simulation, the lens profile is defined by taking points according to these formulae. Two extra points define the the planar surface of the lens. The points are set such that the lens has a thickness of 5 mm in the inner part of the lens. The segmentation of the corrector lens is also implemented in the simulation. The lens is segmented in 24 petals, each with an angular width of 14.735°. The corrector lenses are made of BK7 glass. The optical properties (refractive index and transmittance) of this material are implemented in the Geant4 simulation as a tabulated function of the photon wavelengths. Figure 1.7(a) describes the refractive index of the material while the transmittance for 1 cm of material is shown in figure 1.7(b).

Mirrors

In the TelescopeSimulatorLX the Auger fluorescence telescopes mirrors made of hexagonal elements are implemented in full detail. The mirrors are composed by 64 mirror elements arranged in 8 rows. These elements are quasi-hexagonal spherical mirrors, and their exact shape depends on the position they occupy in the telescope mirror. There are thus different types of mirror elements. The implementation of the mirror elements exploits the Constructive Solid Geometry (CSG) functionalities in Geant4, that allows to build complex solids from simple ones using boolean operations. To build the mirror elements, 3 to 5 (depending on the type of element) trapezoids are joined and the resulting solid is intersected with a spherical shell. The inner radius of the spherical shell is the curvature of the mirror element. Figure 1.8 shows a visualisation of a mirror element. In the left picture the 5 trapezoids

(a) Refractive index of the corrector ring material as a function of the wavelength (λ).
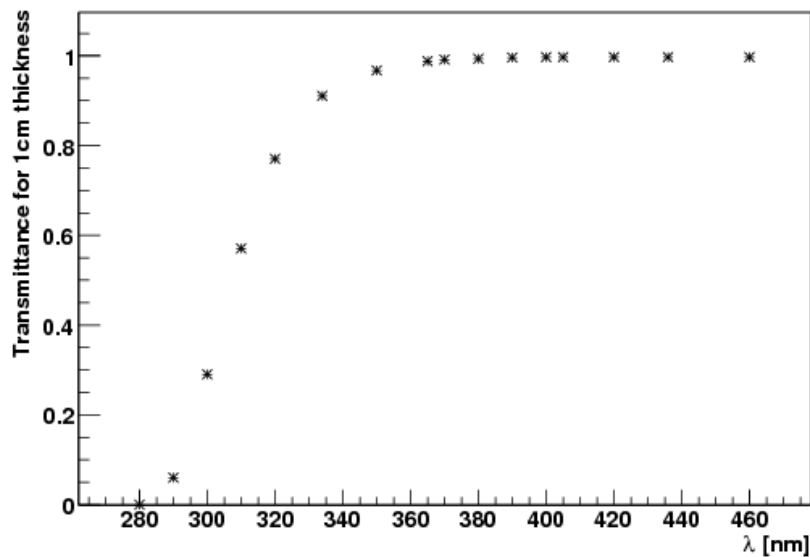
(b) Transmittance for 1 cm of corrector ring material as a function of the wavelength (λ).

Figure 1.7: Optical properties of the corrector ring material.

Figure 1.8: A segment of the Auger FD mirror. Left: the components of the mirror are artificially misaligned to show the internal structure. Right: the mirror segment with all segments properly aligned.

were intentionally misaligned to show the internal structure. Each mirror element is placed according to the vertical and horizontal angles with the vertex, with the alignment point situated in the geometrical centre of the corrector lens. The positioning of the elements emulates the alignment procedure performed in the real telescopes. Each element is placed in such way that the distance from the segment to the alignment point is equal to the segment curvature radius. A visualisation of the complete mirror implemented in the simulation is presented in figure 1.9 . The optical properties of the mirror are implemented by defining the reflectivity in the interface surface between the air and the mirror. The value of reflectivity is constant with the wavelength. The curvature radius, positioning angles and reflectivity are read from an external file containing all the values measured for each segment. An ideal mirror composed of a simple spherical shell is also available in the simulation for testing purposes.

Camera

The camera is composed by the light guides, the photomultipliers and the supporting structure. The light guides are Mercedes stars placed in the vertexes of each photomultiplier. Each Mercedes star is made by the union of three triangular prisms, each built using the Geant4 class G4Polyhedra. The surface interface is defined has having a reflectivity of 0.9 for all wavelengths. A representation of several Mercedes is shown in figure 1.10. The Photomultipliers are hexagons. To simulate the entrance window of the photomultiplier a solid is implemented with a constant refractive index of 1.458. A sensitive detector is placed inside the PMT to simulate
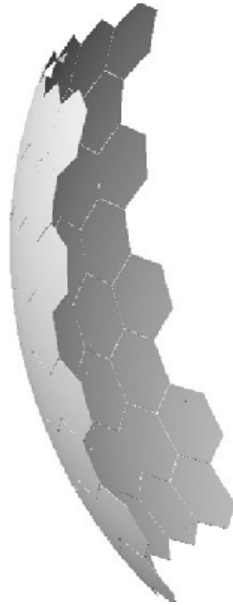
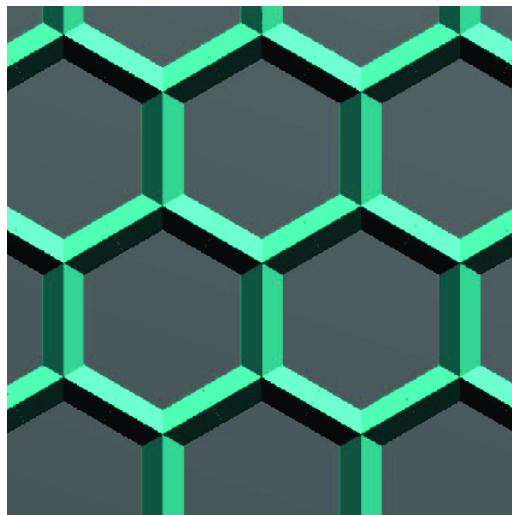Figure 1.9: Visualisation of the Auger FD mirror as implemented in TelescopeSimulatorLX.

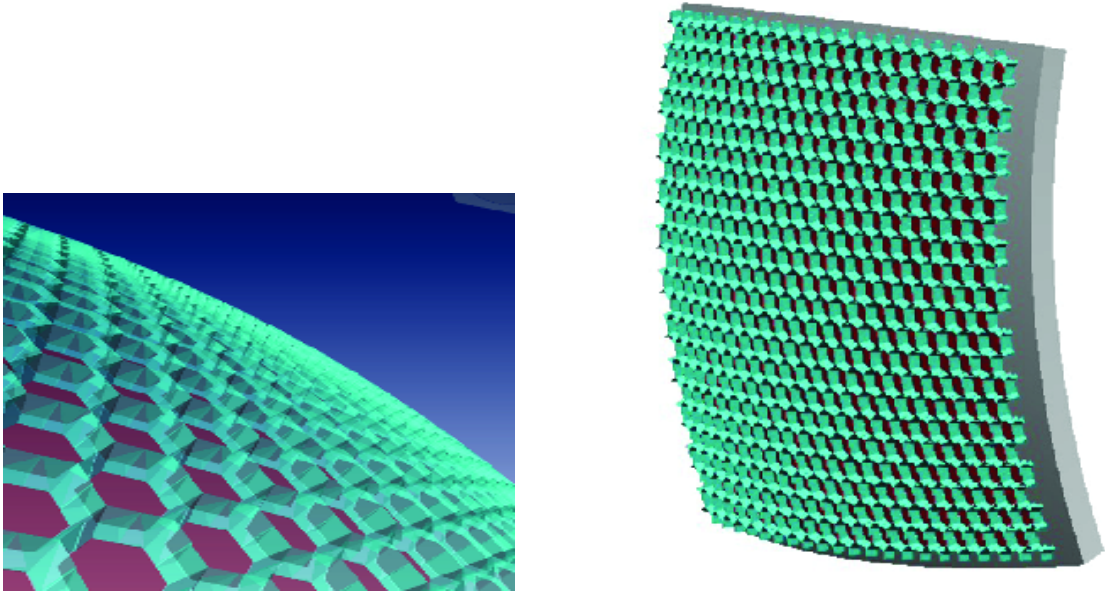Figure 1.10: The Mercedes stars of the Auger FD as implemented in the TelescopeSimulatorLX.

Figure 1.11: The Auger FD camera as implemented in the TelescopeSimulatorLX. Left: detail; Right: the full camera.

the detection of photons in the photocathode. The quantum efficiency is taken into account a posteriori by applying it to the recorded signal at each pixel. Both the PMTs and the light guides are placed following the curvature of the camera. Figure 1.11 shows a visualisation of the camera as implemented in the TelescopeSimulatorLX. On the left, a detail of the camera is shown. On the right, the whole camera is represented, including the camera support in the back of the focal surface. The camera support and feet are implemented to simulate the shadow effect produced due to these elements. A simplified version of the camera is also implemented and used for testing purposes. It consists basically of a spherical surface for the detection of photons placed at the ideal focal surface.

The whole telescope is visualised in figure 1.12. Several sensitive detectors are implemented to allow the passage of photons through the different components of the telescope to be recorded. These sensitive detectors are implemented after the filter, the corrector ring, the mirror and on the ideal focal surface.

A compact version of the module TelescopeSimulatorLX is distributed with the $\overline{\text{Off}}\underline{\text{line}}$. In order to comply with the $\overline{\text{Off}}\underline{\text{line}}$ code policy, this compact version does not implement the output to a separate ROOT file. The output of this version is thus limited to the hits recorded in the PMTs. The other sensitive detectors are not included in this version. Also the visualisation routines are disconnected in this version. The complete version of the module is available upon request.
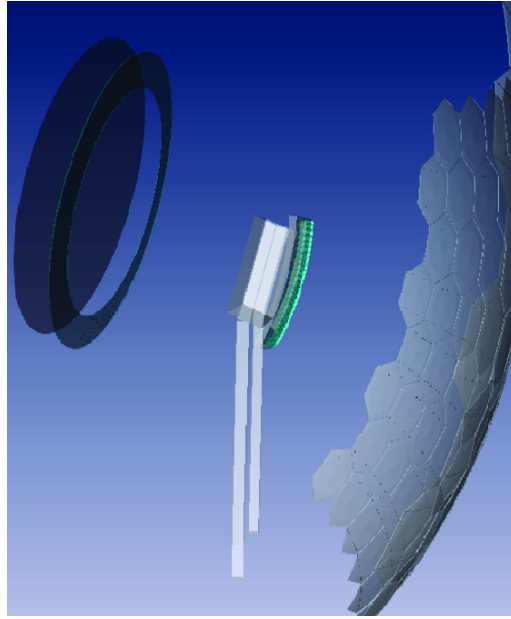
Figure 1.12: The full Auger FD geometry as implemented in the Geant4 simulation in TelescopeSimulatorLX.

1.3 Telescope Performance Evaluation

The simulation tools were used to evaluate the telescope performance. The optical spot and the telescope efficiency were studied using the two available simulation tools.

1.3.1 Simulation Setup

The influence of the optical components is evaluated by characterising the image produced in the ideal focal surface by parallel rays entering the telescope pupil. For this purpose four sets of $100\,000$ photons were generated with input angles of $\theta = 0°, 5°, 10°$ and $15°$ and $\varphi = 135°$. The simulations were performed using the TelescopeSimulatorKG and the TelescopeSimulatorLX codes. The zenithal angle, θ, and the azimuthal angle, φ, are defined in the telescope coordinate system. In this coordinate system the z axis is aligned with the optical axis of the telescope, pointing outwards, the y axis is horizontal and the x axis is orthogonal to the y and z axis, pointing downwards. The origin of this coordinate system coincides with the geometrical centre of the telescope lens.

The position in the camera is defined by the elevation angle, $\alpha = \arcsin\left(x/R_{\mathrm{FS}}\right)$, and the azimuth angle, $\beta = \arcsin\left(-y/R_{\mathrm{FS}}\right)$ where R_{FS} is the radius of curvature of the Focal Surface.

For each generated photon its expected position angles $(\alpha_{\text{expected}}, \beta_{\text{expected}})$ in the ideal focal surface are calculated assuming an ideal optical system. For a given photon, the expected position is calculated as the position that a photon, with the same direction, passing in the centre of curvature of the mirror would have in the camera. Then a relative position, in angle, is calculated. The two new variables are then defined as $\alpha_{\text{rel}} = \alpha - \alpha_{\text{expected}}$, $\beta_{\text{rel}} = \beta - \beta_{\text{expected}}$. This definition has the advantage of measuring the deviation of each photon from the ideal situation.

The angular distance (ζ), to the expected position, of a photon in the Focal Surface can be defined as

$$\zeta = \arcsin\left(\frac{\sqrt{(x - x_{\text{exp}})^2 + (y - y_{\text{exp}})^2}}{R_{\text{FS}}}\right)$$

that can be approximated, for small angles, as

$$\zeta = \sqrt{\alpha_{\text{rel}}^2 + \beta_{\text{rel}}^2}$$

This new variable allows an absolute estimation of the deviation of each photon to the expected position to be obtained.

The position of all photons, simulated using the TelescopeSimulatorLX, in the ideal focal surface of the telescope is represented in figure 1.13. In the figure the position of each photon is marked with a dot in a graph of β versus α. The different colour indicated in the figure represent the different incident angles θ. From the figure it can be seen that there are four spots accompanied by some scattered photons.

1.3.2 The Optical Spot with no Obscuration

The fluorescence telescopes have a completely symmetrical geometry with respect to the optical axis, except for the camera obscuration. In a first step its optical properties were studied when there is no camera. For this study the camera implemented in the Geant4 simulation was replaced by a virtual Focal Surface.

The contribution to the optical spot of the photons that pass through the corrector ring and from the photons that pass through the hollow part of the lens was studied.
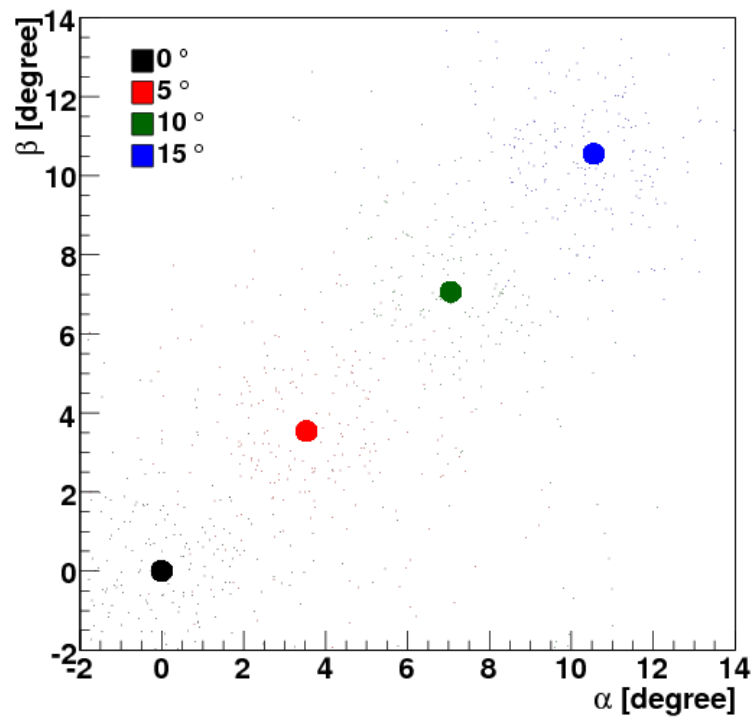
Figure 1.13: Spots produced in the ideal focal surface for incident angles of 0°, 5°, 10° and 15°. The photons were simulated with no camera obscuration. Each photon is represented by a small dot with a colour corresponding to the input direction: 0°- black; 5° - red; 10°- green; 15° - blue.
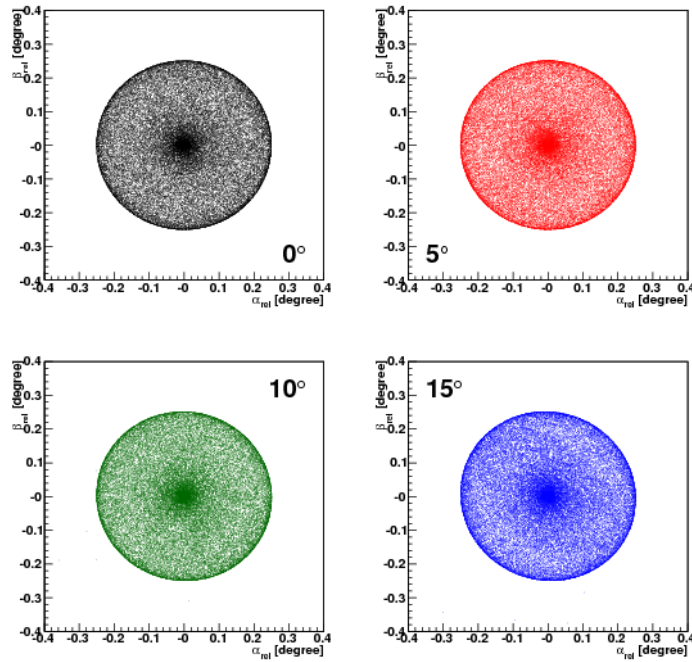
Figure 1.14: Spots produced in the ideal focal surface for incident angles of $0°$, $5°$, $10°$ and $15°$. The photons were simulated with no camera obscuration. For these plots only the photons that do not pass through the corrector lens were selected

Photons with $R_{in} < .85$ (with no corrector ring)

The optical spot produced in the Focal Surface by the photons that do not pass in the corrector ring is presented in figure 1.14. In the figures each photon position, in terms of $(\alpha_{rel}, \beta_{rel})$, is represented by a dot. The photons were selected to have a position in the lens plane with a radius $R < 0.85 \, \mathrm{m}$. The input angles are indicated in the graphs.

The spot is quite featureless, presenting a complete circular symmetry, expected from the complete circular symmetry of the Schmidt telescope (camera excluded). Moreover the spots for the different input angles are very similar, which is also explained by the geometric symmetry of the telescopes.

Photons with $R_{in} > .85$ (with corrector ring)

The contribution from photons that pass through the corrector lens ring is shown in figure 1.15. For the photons with an input angle of $\theta = 0°$ the circular symmetry is maintained. For larger angles the symmetry is lost and the spot is deformed in the same direction as the input direction of the photons. The corrector ring shape depends only on the radius R. However, for inclined photons, the angle between the
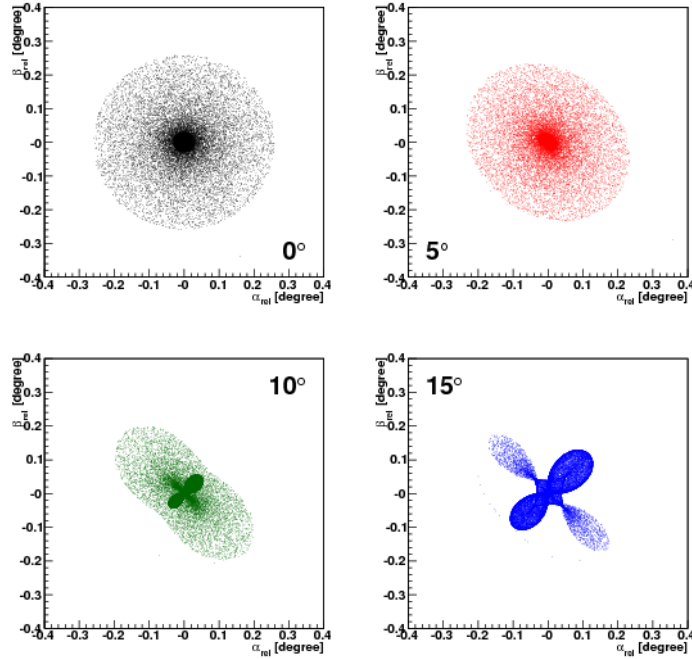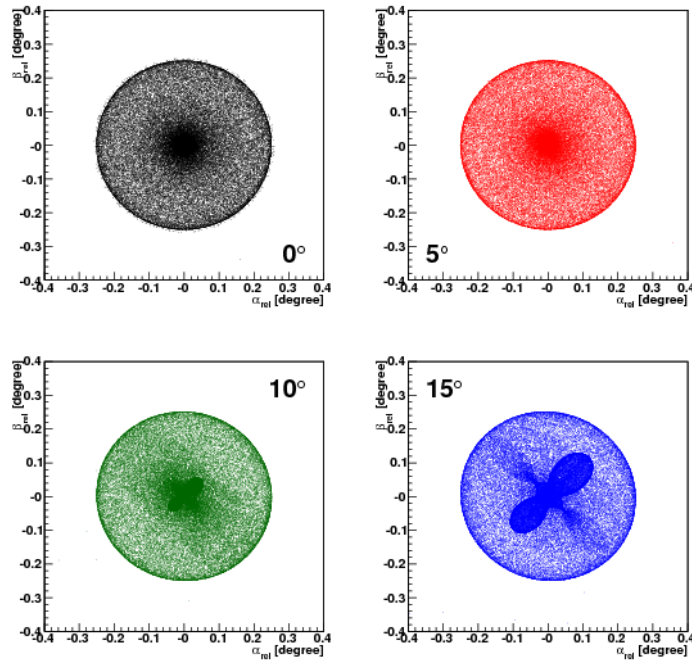
Figure 1.15: Spots produced in the ideal focal surface for incident angles of 0°, 5°, 10° and 15°. The photons were simulated with no camera obscuration. For these plots only the photons that pass through the corrector lens were selected.

1 input photon and the normal to the curved surface has a dependence in φ, for the
2 same R. Thus the correction to the photon angle introduced by the lens will have a
3 dependence with φ, producing the asymmetrical spots seen in figure 1.15.

All Photons

5 The optical spot produced by all the photons passing through the diaphragm at four
6 incident angles are represented in figure 1.16.
7 To have an insight of the dependence of the spot size with the input position
8 of the photons, in the diaphragm, is shown, in figure 1.17, the deviation from the
9 expected position in the focal surface (ζ) versus the input radius of the photon.
10 In the figure it is indicated in grey the zone where the camera shadow will cut
11 the photons and the zone where the input photons pass through the lens. In the
12 region of $0.4 < R_{\text{Diaphragm}} < 0.85$ m, where there is neither camera shadow nor
13 lens, the aberration has a minimum at $R_{\text{Diaphragm}} \sim 0.75$ m and a maximum at
14 $R_{\text{Diaphragm}} \sim 0.45$ m. The later one is translated in figure 1.14 by the clear cut on
15 the spot edge. It is also seen that the aberration starts to rise quite rapidly from
16 the minimum with the input radius having a value of $\sim 0.23°$ for an input radius

Figure 1.16: Spots produced in the ideal focal surface for incident angles of 0°, 5°, 10° and 15°. The photons were simulated with no camera obscuration.

of $R_{\text{Diaphragm}} = 0.85$ m. For a fluorescence telescope with no corrector ring and a radius of 0.85 m the maximum aberration would be then given by the maximum at $R_{\text{Diaphragm}} \sim 0.45$ m. However, if the aperture radius were to be increased without the introduction of a corrector ring the aberration would continue to rise quite rapidly taking a value of $\zeta \sim 1.375°$ for a radius of 1.1 m. This aberration value corresponds to a spot with a radius of about 42 mm. The introduction of the corrector ring increases the pupil area of the telescope from $2.27\,\text{m}^2$ to $3.80\,\text{m}^2$ (67% increase) maintaining the aberration of the telescope. However, taking into account the reduction due to the camera shadow of about 0.8 m², that is present in both cases, the collection area is doubled from $1.47\,\text{m}^2$ to $3.00\,\text{m}^2$.

1.3.3 Obscuration Effects

The shadow of the camera plays an important role in the fluorescence telescope, reducing the collection area by a factor greater than 20%. Moreover the square shape of the camera breaks the symmetry of the optical system. The camera, its body and support structure are described in detail in the TelescopeSimulatorLX module. Figure 1.18 presents the spot for different input angles when the camera shadow is taken into account in the simulation. The contribution to the spot shape
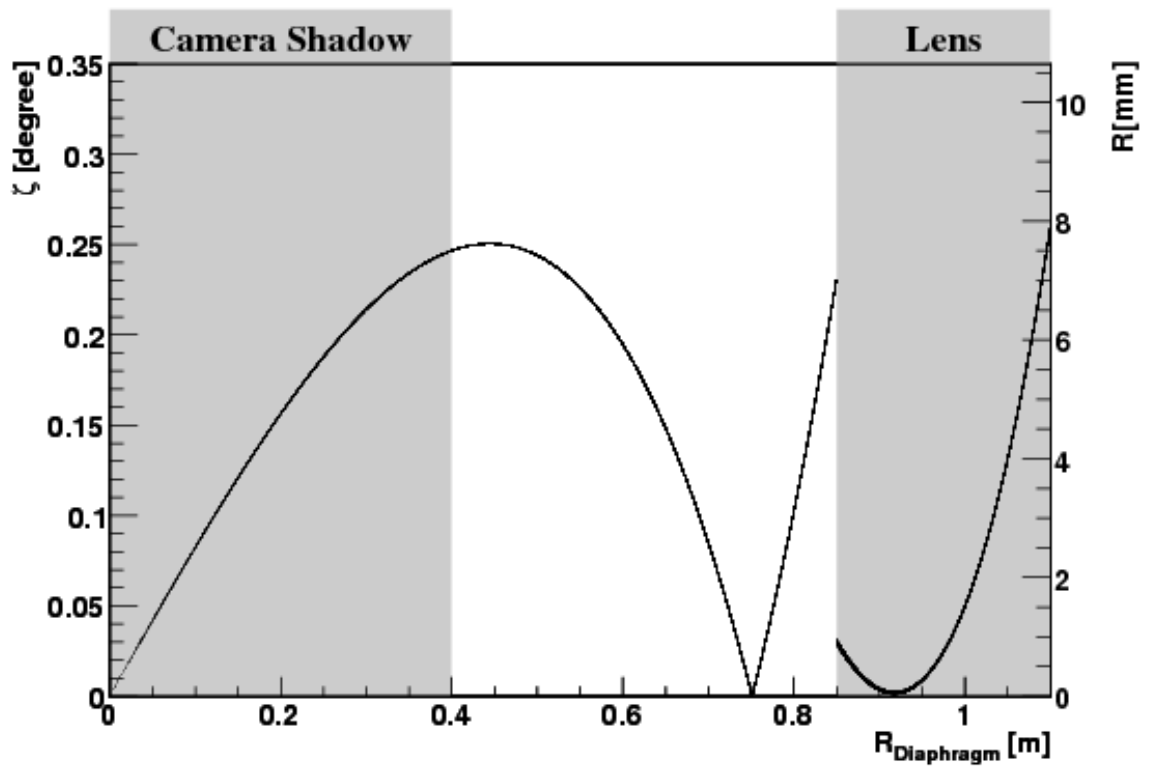
Figure 1.17: Deviation from the expected position in the focal surface in angle, ζ, as a function of the input radius, $R_{\text{Diaphragm}}$. The camera and lens zone are indicated in grey. Photons were generated with incident angles of $0°$.
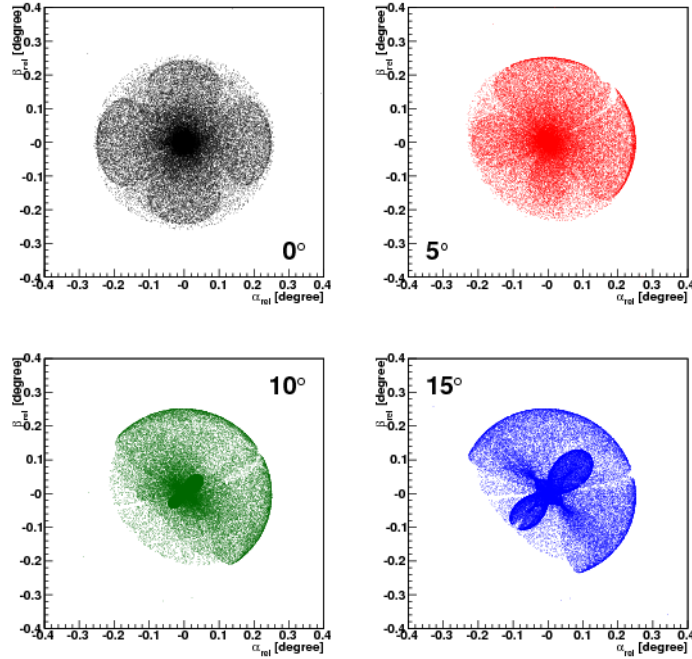
Figure 1.18: Spots produced in the ideal focal surface for incident angles of 0°, 5°, 10° and 15°. The camera obscuration was simulated.

from the photons that pass through the hollow part of the lens and from the photons that pass through the corrector ring are presented in figure 1.19 and figure 1.20, respectively. To better understand the camera shadow it is plotted in figure 1.21 the position of the photons in the mirror, in $(\alpha_{\rm rel}, \beta_{\rm rel})$, for the four simulated input angles. The shadow of the camera produces the white hole seen in the figures. The square part corresponds to the camera body while the two "thick lines" correspond to the legs that support the camera in place. The photons that pass through the lens are represented in red while the others are plotted in black. For the input angles of 0°and 5° it is seen that the camera shadow only affects the photons that pass through the hollow part of the lens. For 10°and 15° some of the photons that pass through the corrector ring are shadowed. However the percentage of photons killed is smaller for these photons than for the ones that pass by the hole in the lens.

From figure 1.18 it is clear the asymmetry introduced by the camera obscuration reflected in the spots shape. From the two plots where the contribution to the spot is separated it is clear that most of the asymmetry arises from the photons that pass through the hollow part of the Lens. It is also seen in figure 1.19 that for higher input angles there is a reduction of the photon density in a quarter to a half spot. This introduces a shift on the barycentre of the spot. However this shift is very small since the centre of the spot has a very high density of photons.
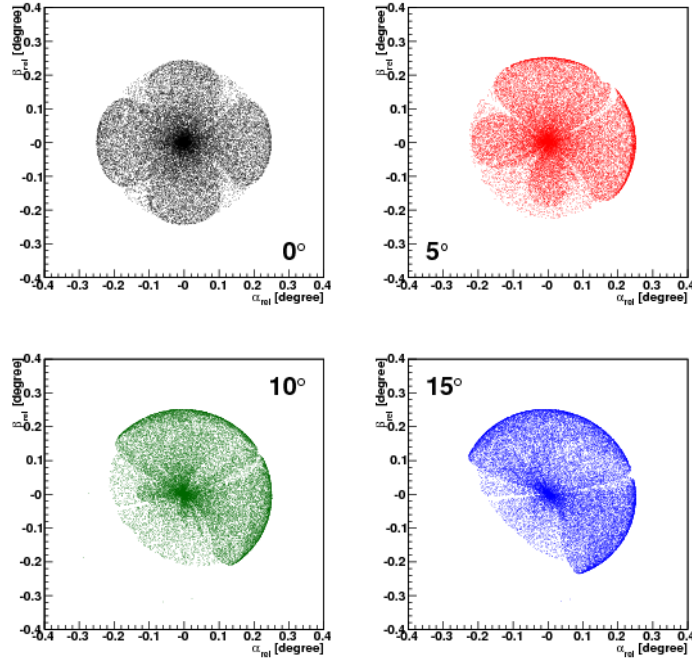
Figure 1.19: Spots produced in the ideal focal surface for incident angles of 0°, 5°, 10° and 15°. The photons were simulated with camera obscuration. For these plots only the photons that do not pass through the corrector lens were selected
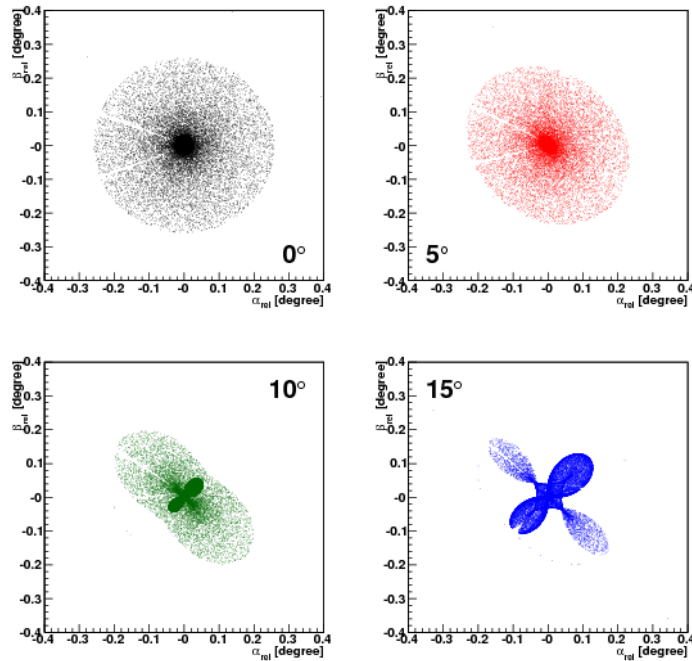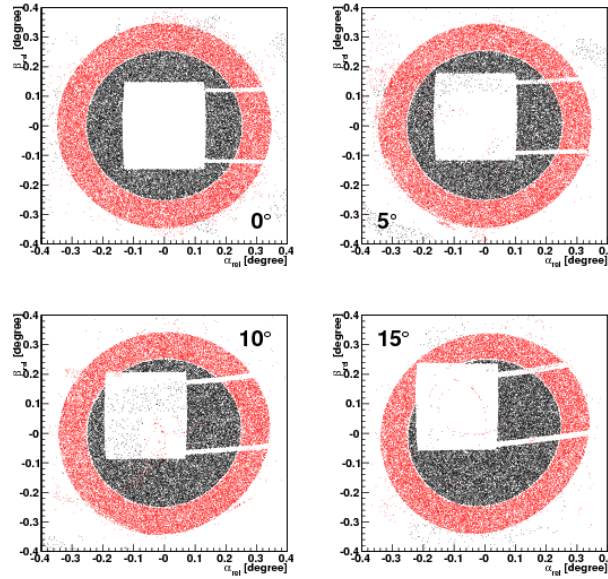

Figure 1.20: Spots produced in the ideal focal surface for incident angles of 0°, 5°, 10° and 15°. The photons were simulated with camera obscuration. For these plots only the photons that pass through the corrector lens were selected.

Figure 1.21: Photons in the mirror for incident angles of 0°, 5°, 10° and 15°. The photons were simulated with camera obscuration. The photons that pass through the hollow part of the lens are plotted in black while the photons that pass through the lens are plotted in red.

1.3.4 Spot Size

The simulations produced were used to study the spot size at the focal surface. The effect of the lens on the spot size and its dependence with the lens profile and incidence angle were evaluated.

The Effect of the Corrector Ring

Figure 1.22 represents the distributions of ζ for the photons in the ideal focal surface for photons simulated with the TelescopeSimulatorLX (solid lines) and the TelescopeSimulatorKG (dashed lines). For each simulation the distribution of the photons that pass through the hollow part of the lens is represented in red and for the photons that pass through the lens in blue. The distribution for all detected photons is represented in black. From the left plot it is evident that most of the photons lie in the region of $0° < \zeta < 0.25°$. However, for the TelescopeSimulatorLX, there are a small fraction of photons that have higher ζ in the focal surface up to 6.2°. The photons with $0.25° < \zeta < 6.2°$ represent a fraction of 0.34% of the total number of photons. From the figure it can also be seen that all of these photons pass through the corrector ring. It was also seen from the simulation that these photon give hits in the filter with a different position than the one they were generated with.
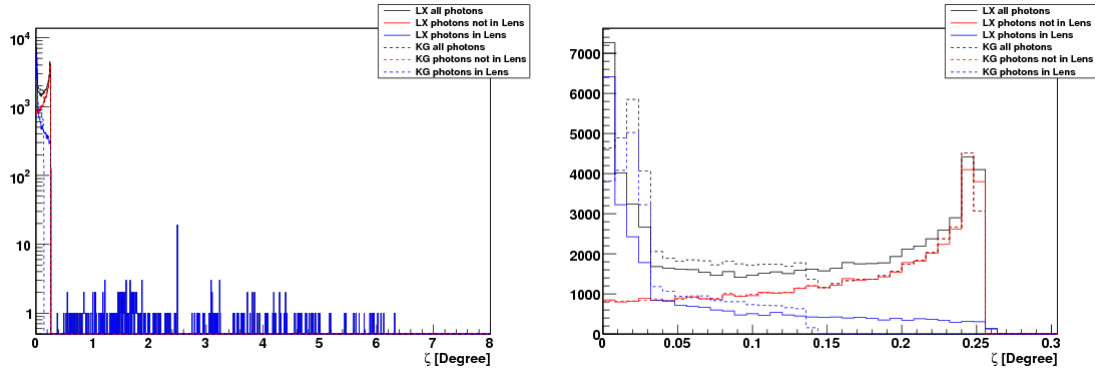
Figure 1.22: Distribution of ζ for the photons in the ideal focal surface. The right plot is a zoom of the left one in the range $0° < \zeta < 0.30°$

This facts suggest that these photons are reflected in the lens, coming back to the filter and then reflected again. In the right plot it was made a zoom to region of $0° < \zeta < 0.30°$. In the figure it can be seen that there is a good agreement in the simulation of photons that pass through the hollow part of the lens. The agreement is not so good for the photons that do pass in the lens and this is reflected in the overall distribution. To better understand the spread of the photons in the focal surface, the cumulative distribution of ζ is drawn in figure 1.23. The curves follow the same colour scheme of the previous image. In this figure the cumulative curves for all detected photons are normalised to 1. The curves for individual contributions are normalised to one over the total number of detected photons to represent the relative contribution to the overall cumulative curves. A horizontal dashed line is drawn to indicate 0.9 of the cumulative distribution, allowing the size of the spot that contains 90% of the photons to be easily estimated. In the figure it can be seen the good agreement between the two simulations for the photons that do not pass through the lens. The two simulation show a difference for the photons that pass through the lens which is reflected in the cumulative curve for all detected photons up until $\zeta < 0.25°$. Although the two simulations present such difference the spot size, that contains 90% of photons, is in both simulations equal to $0.24°$.

Dependence with the Corrector Ring Profile

The corrector ring plays an important role on the fluorescence telescope. The shape of the lens influences directly the spot shape and thus the performance of the telescope. To study the spot shape the TelescopeSimulatorLX was used to simulate four sets of photons, each with 100 000 photons, with an input angle $\theta = 0°$ and different lens profiles. The cumulative curves for the different profiles are shown in figure

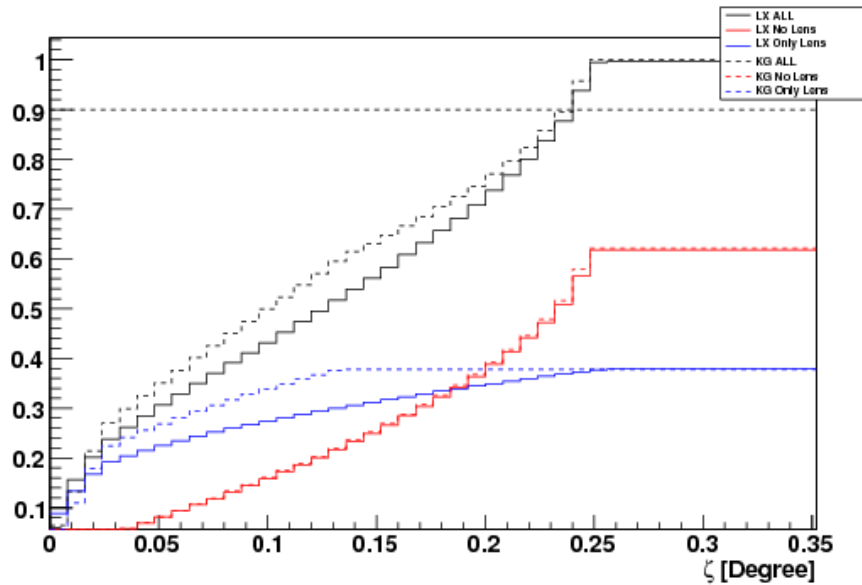Figure 1.23: Cumulative curves of ζ for the photons in the ideal focal surface simulated with the TelescopeSimulatorLX (solid) and the TelescopeSimulatorKG (dashed). The contributions of the photons that pass through the lens (red) and the photons that pass through the hollow part of the lens (blue) are represented as the overall (black) cumulative curve.

1.24 . In a dashed black line the cumulative curve obtained using the TelescopeSimulatorKG simulation code is represented. The solid lines were obtained using the TelescopeSimulatorLX simulation code. The profiles used correspond to the "KG" profile (in black), the "circular" profile (in red), the "upper limit" (in blue) and "lower limit" (in green) profiles. The first thing to note in the figure is that the two simulation codes are in agreement, provided that the TelescopeSimulatorLX uses the profile implemented in the "KG" code. The cumulative curves have small variations, apart from the "upper limit" curve, showing values for the spot size, at 90%, in the range $0.20° < \zeta < 0.22°$. The curve for the "upper limit" shows a spot size of $\zeta = 0.24°$. However at a $\zeta \sim 0.25°$ the curves seem to converge. This indicates that if the spot size is defined to include 99% of the photons there is very small variation of the spot size with the lens profile.

The Effect of the Gaps in the Corrector Ring

Due to the large size of the corrector lenses (2.2 m outer diameter) they had to be manufactured in pieces. In the design [3] it is specified that each lens was sectioned in 24 segments of 15°. However, in situ, it was observed that the gaps between the segments were not regular and could, in the worst case, amount to several
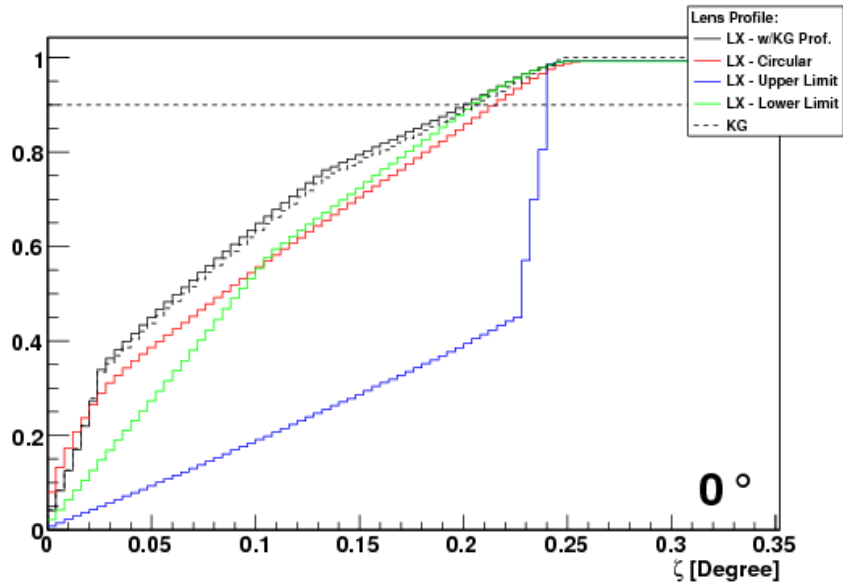
Figure 1.24: Cumulative curves of ζ for the photons in the ideal focal surface simulated with the TelescopeSimulatorLX. Black - "KG" profile; Red - Circular profile; Blue - "Upper Limit" profile; Green - "Lower Limit" profile. A dashed black curve represents the cumulative curve simulated with the TelescopeSimulatorKG code.

centimetres. The effect of these gaps on the spot in the focal surface was studied using the TelescopeSimulatorLX code. In face of the lack of measurements of these gaps, the gaps were implemented by reducing, evenly, the covered angle of each segment to 14.735° and equally spacing the 24 segments.

The Spot produced by an unsectioned corrector ring is shown in the left image of figure 1.25 while in the right image the spot produced using the sectioned corrector ring is shown. It is evident that a star-like effect appears in the spot. Photons lying in the "arms" of this star are photons that passed through the gaps of the corrector lens and its direction was thus not corrected by the lens. These photons have a maximum deviation from the expected position of $\sim 1.5°$ which corresponds to the spot size that would be obtained if the corrector ring was not used. However, the fraction of "uncorrected" photons is small and corresponds to the area of the gaps over the total pupil area that amounts to $\sim 0.7\%$.

Dependence with Incidence Angle

The dependence of the spot size with the input angle, and different simulations, is studied by plotting the respective cumulative curves in figure 1.26. In the figure the solid lines are obtained using the TelescopeSimulatorLX code while the dashed
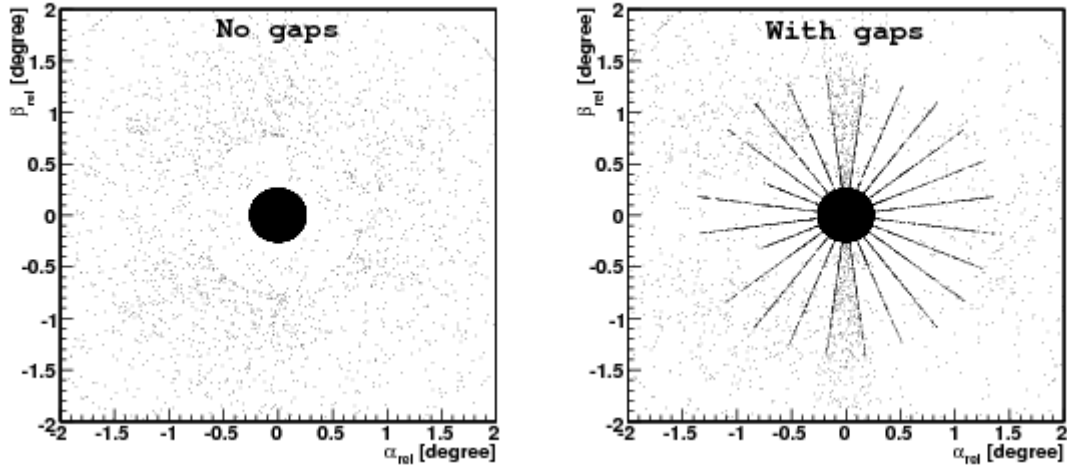
Figure 1.25: Spots produced in the ideal focal surface. The left image was obtained by simulating the corrector ring without gaps. In the right image the corrector ring was sectioned in 24 segments of 14.735°.
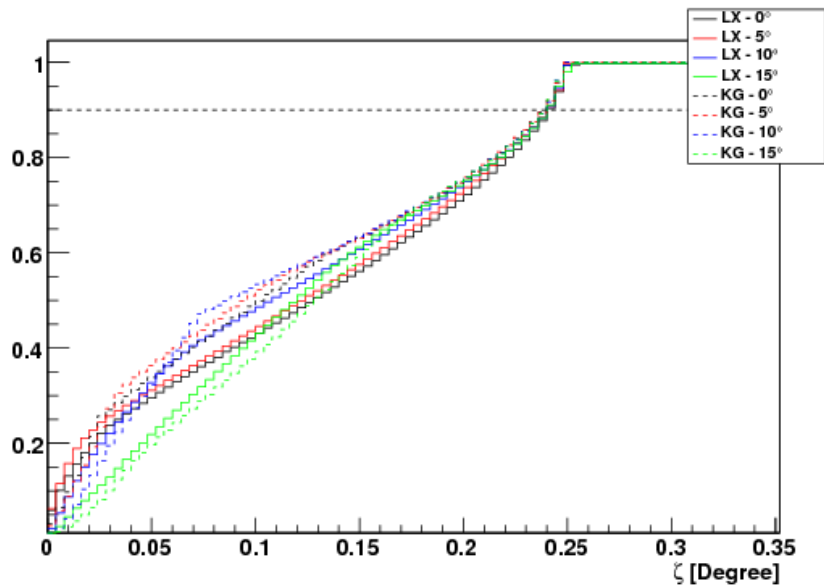

Figure 1.26: Cumulative curves of ζ of the photons in the focal surface simulated with the TelescopeSimulatorLX (solid) and TelescopeSimulatorKG (dashed). The input photons have input angles of 0° (black), 5° (red), 10° (blue) and 15° (green).

lines are for the TelescopeSimulatorKG code. The curves for photons with input
angles, θ, of 0°, 5°, 10° and 15° are respectively represented in black, red, blue and
green. As expected from the previous figure there are small differences between the
cumulative curves using the TelescopeSimulatorLX and the TelescopeSimulatorKG.
Moreover the shape of the cumulative curve, and thus the spot shape, varies with
the input angle. However the spot size, at 90%, does not vary with the input angle
and simulation code.

1.3.5   Photon Distribution in the PMTs

Photons in the focal surface propagate reaching the Photomultipliers placed behind.
The inefficiency areas between the PMTs are overcome by the use of the Mercedes
stars where the photon reflects to a PMT. In figure 1.27 the position of the photons
in the PMT are represented. In the top figures, 1.27(a) and 1.27(b), each photon is
represented by a dot. Black dots represent the photons that hit a PMT directly while
the blue dots represent photons that have at least one reflection in the Mercedes
before hitting the PMT. Red dots represent the last reflection in the Mercedes for
photons that will reach a PMT while the green dots represent the same for photons
that aren't collected in a PMT after reflecting. A violet circle with a radius of 0.25°
is drawn as a reference to indicate the spot size in the focal surface. In the bottom
figures, 1.27(c) and 1.27(d), are presented histograms where the photon density is
represented in a logarithmic colour scale with the same range. In all figures solid
blue lines are drawn to indicate the pixel boundaries and dashed ones to indicate the
Mercedes boundaries. The figures in the left were obtained by simulating photons
with an expected position in the centre of a pixel. The input directions were set
with $\theta = 0.866°$ and $\varphi = 0°$. On the other hand the photons in the right plots were
generated with $\theta = 0°$ in order to have an expected position in the centre of the
camera and thus in the vertex of a Mercedes star.

The first fact to notice from the figures is that the spot is larger in the PMT than
in the Focal Surface. This is due to the fact that the photons reach the focal surface
with large incident angles. This can be seen from figure 1.28 where the distribution
of the incident angles for the photons that hit the focal surface is plotted. The
photons in the figure were generated with an input angle $\theta = 0°$. The gap in the
plot at an incident angle of $\sim 29°$ is directly related to the low photon density in
a circular zone in the mirror seen in figure 1.21 which, in turn, derives from the
internal border of the corrector lens. As the PMTs are recessed by ~ 18 mm, the
height of the Mercedes light guides, a photon with an incident angle of 30° deviates,

(a) Photons directed to pixel center

(b) Photons directed to mercedes center

(c) Photons directed to pixel center
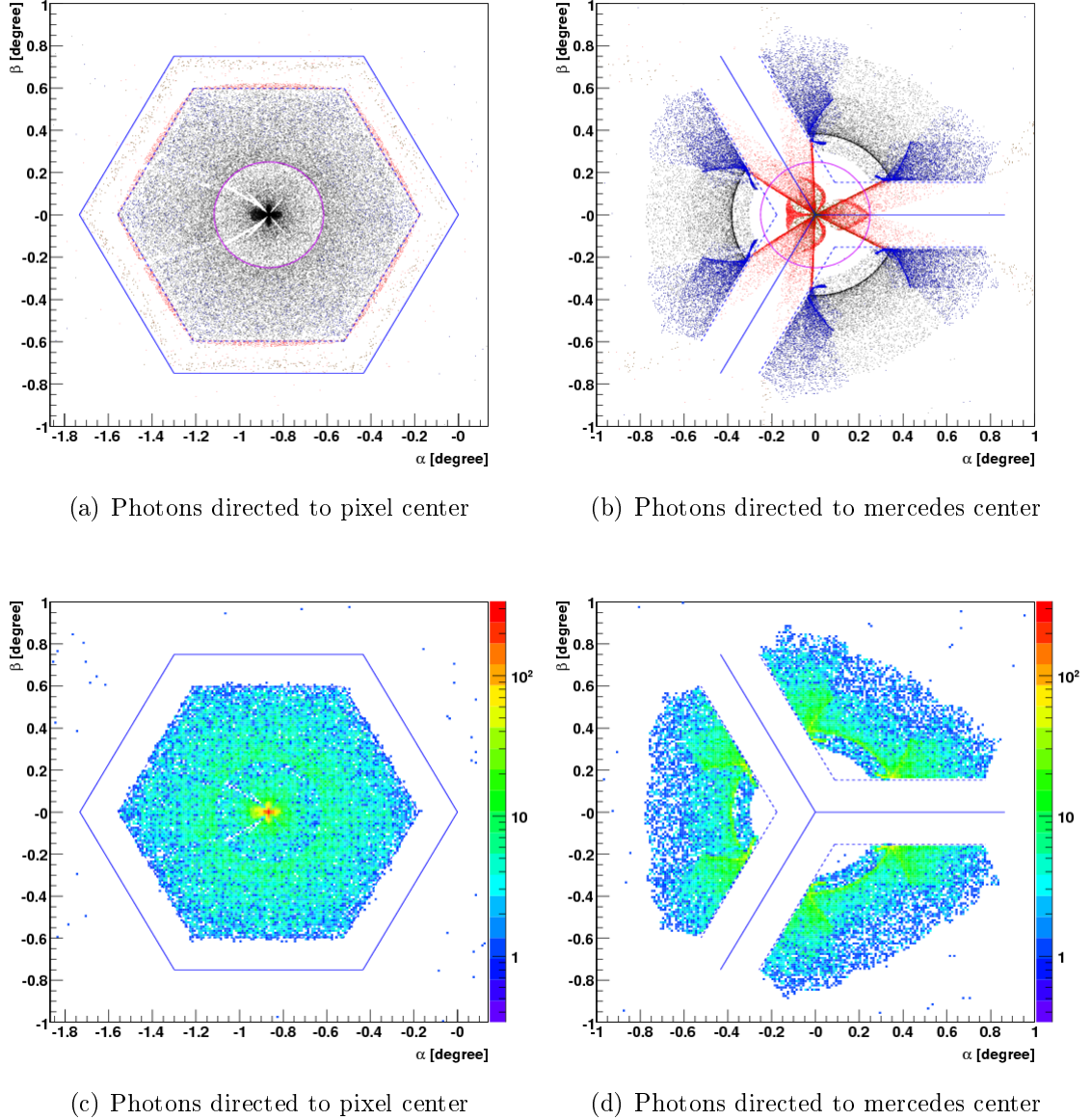
(d) Photons directed to mercedes center

Figure 1.27: The spot seen in the PMTs. Top figures are scatter plots of the position of the photons. The photons that hit directly the PMT are represented in black while in blue are represented the photons that have at least one reflection in the Mercedes before hitting a PMT. In red is represented the last hit in the Mercedes. In green are represented the hits in the Mercedes for photons that do not hit a PMT. A violet circle with a radius of 0.25° represents the size of the spot in the focal surface. Bottom figures are histograms of the photon density in the PMT. The density is indicated by a logarithmic colour scale. In all figures blue lines are drawn to represent the pixel boundaries (solid) and the Mercedes boundaries (dashed).
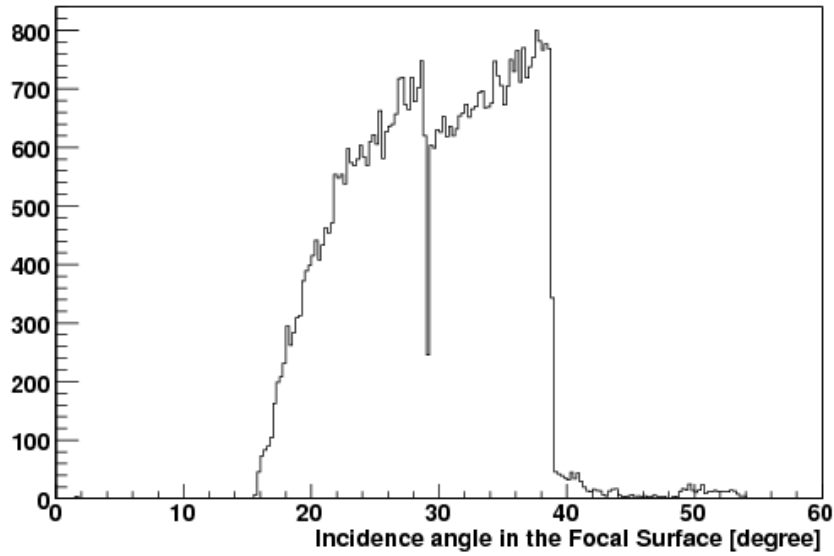
Figure 1.28: Distribution of the incident angles for the photons that arrive to the ideal focal surface for photons generated with an input angle $\theta = 0°$.

1 horizontally, approximately 10 mm from its position in the focal surface.

2 Despite this enlargement, the spot in the left images of figure 1.27 is contained

3 inside the pixel with few hits on the Mercedes and consequently few photons hitting

4 the PMT with a previous reflection on the Mercedes. From the bottom left histogram

5 it can be seen that there is a high density region in the centre of the pixel.

6 When the photons are directed to the Mercedes centre the three adjacent PMTs

7 are hit. It can be seen from figure 1.27(b) that there is a direct component of hits in

8 the PMT that is enlarged as in the previous case. However there is a large fraction

9 of photons reflected in the Mercedes. These photons hit the PMT in very specific

10 zones near the Mercedes, seen in the figure by the high density zones of blue dots.

11 It can also be seen that the photons that do not reach a PMT are in the central

12 region of the Mercedes. The figure 1.27(d) shows the density of photons in the PMT

13 and is drawn using the same colour scale and range as the left one. It can be seen

14 that there is no region with such high density as the central region in the bottom

15 left figure. Also it can be noticed that there is some kind of a circle, centred in the

16 Mercedes vertex, where there are no photon hits in the PMT. This is due to an effect

17 of shadowing of the Mercedes star. The density of photons has a circular symmetry

18 around the centre of the Mercedes. The highest density of photons is located near

19 one of the vertexes of the hexagonal PMT.

20 Regarding the efficiency there are some differences between the two studied cases.

When the photons are directed to the pixel centre, 1.7% of the photons are lost after reflecting in a Mercedes. On the other hand, when the photons are directed to the Mercedes vertex, this number rises to 4.4%. The overall efficiency, defined as the number of photons detected in a PMT over the number of photons in the focal surface is of 94% and 88%, respectively. Part of this efficiency reduction is explained by the decrease of the number of photons arriving on the PMT window after reflection in a Mercedes. The other part is probably due to reflections in the PMT window before hitting the photocathode of the PMT. The reflection probability depends on the impinging angle and thus different configurations can lead to different efficiencies.

From the two cases studied it can be concluded that the "illuminated" zones of the PMTs vary with the position of the spot centre. The collection efficiency of a PMT varies with the distance to its centre. Such dependency influences the overall telescope efficiency with the spot centre position. If necessary, the effect can be easily taken into account in the TelescopeSimulatorLX simulation code, if a model of the PMT efficiency dependence with the radius is provided.

1.3.6 Telescope Efficiency

The optical efficiency of the telescope results from the convolution of the different efficiencies of the optical components and relates the number of photons that are able to reach the focal surface with the number of collected photons. The efficiency was evaluated using the simulations described before. The efficiency is then defined as the ratio between the photons that arrive to the focal surface and the generated photons:

$$\varepsilon = \frac{N_{\mathrm{FS}}}{N_{\mathrm{generated}}}$$

In figure 1.29 the optical efficiency of the fluorescence telescope is presented as a function of the input radius at the diaphragm ($R_{\mathrm{Diaphragm}}$) for photons with a direction perpendicular to the input pupil. The curves represent the efficiency obtained using the TelescopeSimulatorKG (red) and the TelescopeSimulatorLX (blue) and the efficiency obtained if the requirement that the photons fall inside a circle such that $\zeta < 0.27°$ for the TelescopeSimulatorKG (orange) and for the TelescopeSimulatorLX (violet). The red curve is not visible as it is overlapped by the orange one. In the region where $0 < R_{\mathrm{Diaphragm}} < 0.4\,\mathrm{m}$ all the photons are killed by the shadowing of the camera. For higher input radius the efficiency curve grows as the camera is square shaped and the fraction of photons killed is reducing until the efficiency of the system is given by the convolution of the filter transmittance and the mirror reflec-
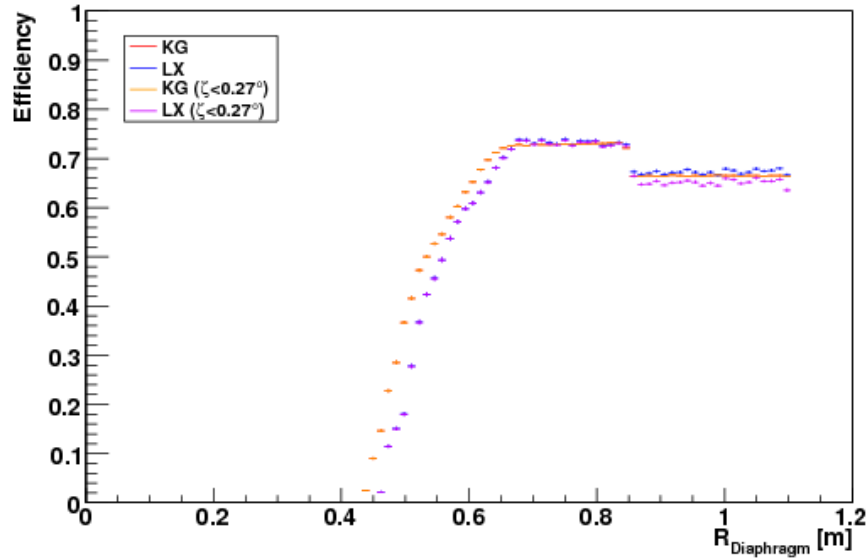
Figure 1.29: Telescope efficiency versus the radius at the diaphragm of incident photons. The photons were generated with an incident angle $\theta = 0°$.

tivity. For $R_{\mathrm{Diaphragm}} > 0.85$ m the photons pass through the corrector lens and its inefficiency causes the global efficiency to drop. It is probable that the camera structure has slight differences in its description on the two simulation codes, producing slightly different obscurations of the camera which is translated in a difference on efficiency in the region where $0.4 < R_{\mathrm{Diaphragm}} < 0.7$ m. The overall efficiency for the two simulation codes is estimated as 54.17% for the TelescopeSimulatorKG and 53.11% for the TelescopeSimulatorLX representing a difference of $\sim 1\%$. The spots generated using the TelescopeSimulatorLX code have a small component of photons with high ζ that will be considered as noise in the analysis of the events. Discarding the photons with a $\zeta > 0.27°$ reduces the optical efficiency to 52.22%, representing a reduction of $\sim 1\%$.

Figure 1.30 is equivalent to the previous one but the photons have an input angle of $\theta = 10°$ at the entrance pupil. In this case there are evident differences between the two simulation codes used in the regions where the photons start to enter the corrector ring of ($R_{\mathrm{Diaphragm}} \sim 0.85$ m) and near the end of the diaphragm ($R_{\mathrm{Diaphragm}} \sim 0.85$ m). This difference is explained by the fact that in the TelescopeSimulatorLX the filter, a circle that defines the input pupil and has the same size of the corrector ring, is placed, following the specification design and confirmed on site, 10 cm before the corrector lens and thus 10 cm before the centre of curvature of the mirror. In the TelescopeSimulatorKG the filter is placed in the plane of the
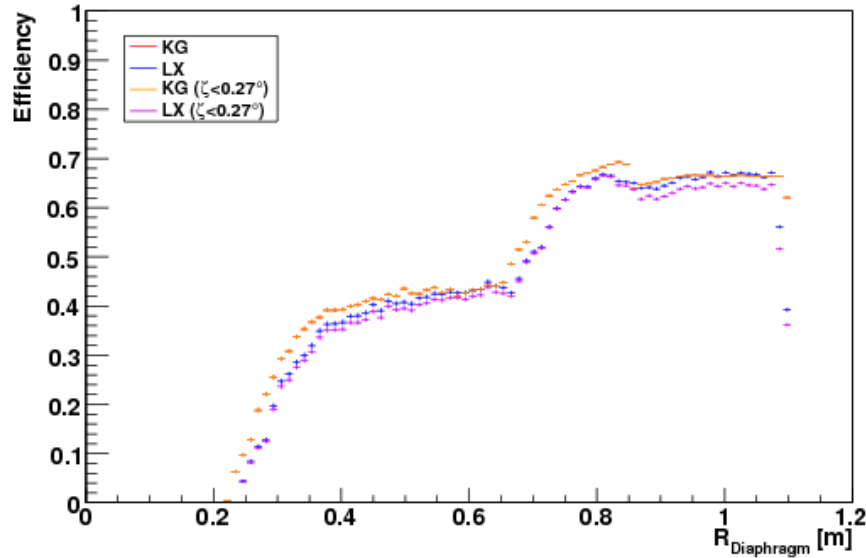
Figure 1.30: Telescope efficiency versus the radius at the diaphragm of incident photons. The photons were generated with an incident angle $\theta = 10°$.

1 lens. Thus, in the TelescopeSimulatorLX, there is an effect of a projection of the
2 pupil circle in the lens circle, reducing the collection area for inclined photons. The
3 overall efficiency for the two simulation codes is, in this case, estimated as 53.83% for
4 the TelescopeSimulatorKG and 51.63% for the TelescopeSimulatorLX representing
5 a 2.2% difference. Moreover if the cut at $\zeta < 0.27°$ is imposed, the efficiency using
6 TelescopeSimulatorLX would be of 50.28%, representing a reduction of $\sim 1.4\%$.

7   A test was performed, placing in the TelescopeSimulatorLX the filter near the
8 lens. The resulting curves for the efficiency are shown in figure 1.31 . It is clear
9 that the differences between the simulations are reduced. In this test the overall
10 efficiency, estimated with the TelescopeSimulatorLX yields a value of 52.29%, if all
11 photons are considered, which represents a reduction of $\sim 1.5\%$. If only photons
12 with $\zeta < 0.27°$ are considered an efficiency of 50.89% is obtained which represent a
13 reduction of 1.4%.

14   Two spots images are shown in figure 1.32 where it is evident a component at
15 large angles. One million photons were simulated with the TelescopeSimulatorLX
16 with input angles of $\theta = 0°$ (left) and $\theta = 10°$ (right). The spot appears, in both
17 cases, in the expected position with its star structure due to the corrector ring gaps.
18 In the first case, $\theta = 0°$, the photons with $\zeta > 0.27°$ amount to 8898 and the ones
19 with $\zeta > 8°$ to 72 (of 10^6 generated photons). In the second case, $\theta = 10°$, the spot
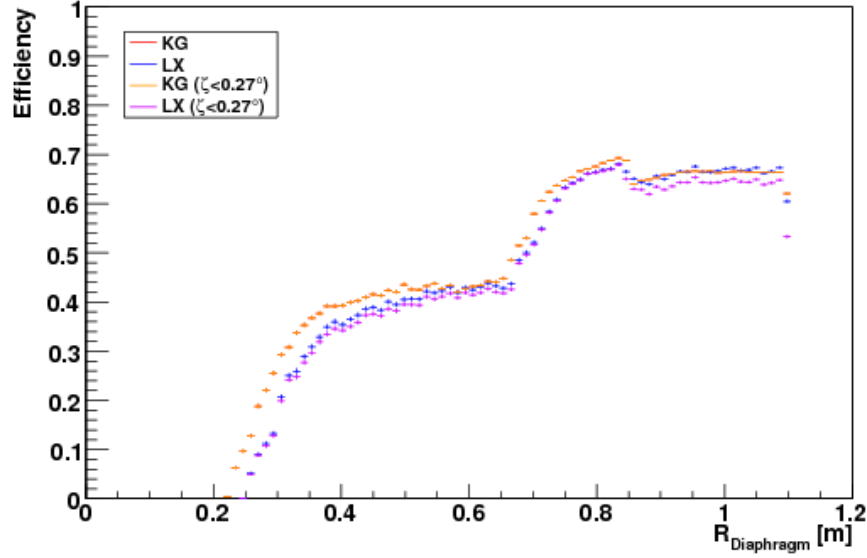20 image presents additional structures besides the spot centred at $(\alpha, \beta) = (7°, 7°)$.

Figure 1.31: Telescope efficiency versus the radius at the diaphragm of incident photons. The photon were generated with an incident angle $\theta = 10°$. The filter was placed close to the corrector lens in the TelescopeSimulatorLX
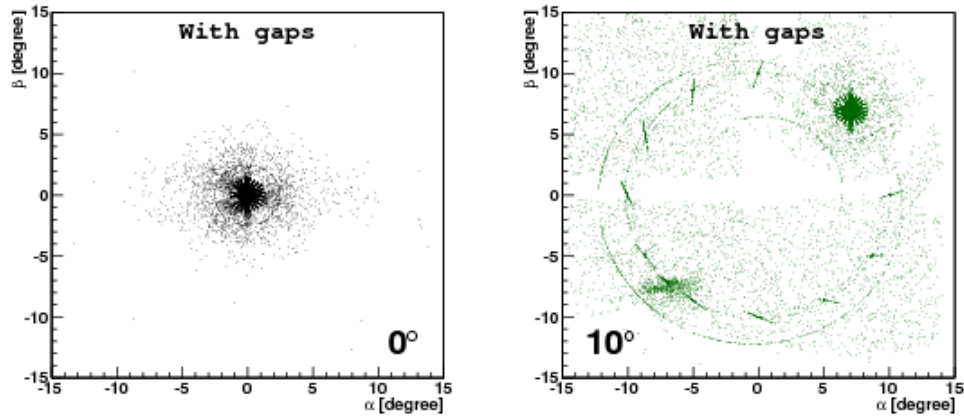

Figure 1.32: Spots in the focal surface simulated with the TelescopeSimulatorLX. Photons were generated with an input direction $\theta = 0°$(left) and $\theta = 10°$.
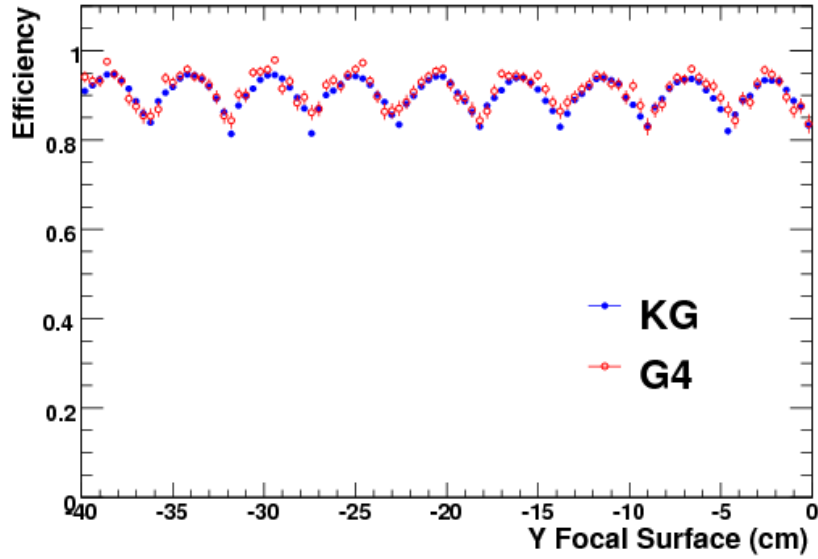
Figure 1.33: Efficiency versus the horizontal position in the camera.

Two circumferences, some lines and also a ghost spot at $(\alpha, \beta) \sim (-7°, -7°)$ appear. The circles and lines are related to reflections in the lens segments surfaces. The ghost spot is the result of photons that get reflected in the camera, travel back to the lens and/or filter where they are reflected and imaged again in the camera. The photons that are imaged with $\zeta > 0.27°$ amount to 13449 and the ones with $\zeta > 8°$ to 7327 (of 10^6 generated photons).

   The efficiency of the Mercedes and PMT was evaluated by simulating photons with random incidence direction in order to illuminate the whole camera. A thin strip in the centre region was then selected. The photons in this strip were used to plot the efficiency as a function of the horizontal position in the camera. This plot is seen in figure 1.33. The zones of higher efficiency correspond to the photons arriving directly to the PMTs and the low efficiency zones are due to the reflections in the Mercedes before hitting the PMTs.

1.4 Comparison Between Simulation and Data

1.4.1 Comparison with Laboratory Data

Using TelescopeSimulatorLX, the uniformity measurements described in [9] were simulated. In this measurement, a small version of the camera with seven pixels was used. In the absence of an optical system, the optical conditions of the Auger
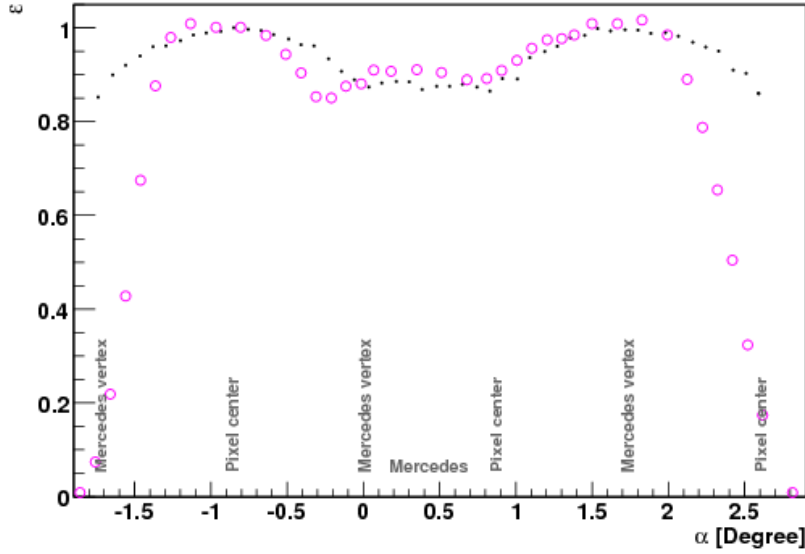
Figure 1.34: Relative efficiency along a vertical line passing through Mercedes vertexes. The black dots are the simulation results and the white circles are the measurements from [9].

FD were approximately reproduced by diffusing the light from a Xenon flash lamp inside a cylinder made in such a way that the realistic angles of incidence in the camera were obtained (approximately between $10°$ and $30°$, due to the shadow of the camera and the aperture of the diaphragm, respectively). Since the FD optics is fully simulated with Geant4, this setup is easily simulated using TelescopeSimulatorLX by fully illuminating the diaphragm with parallel light rays with incident directions such that a scan of the seven central pixels was performed.

As in [9], two scans, one passing over the Mercedes arms and one passing over the Mercedes vertexes, were performed. The position of the photons in the camera is defined here by the elevation angle, $\alpha = \arcsin(x/R_{FS})$, and the azimuth angle, $\beta = \arcsin(-y/R_{FS})$ where R_{FS} is the radius of curvature of the focal surface. The efficiency is defined as the ratio between the number of photons that arrive at the PMTs and the number of generated photons. The efficiencies are normalised to the efficiency value in the centre of the central pixel. The results are shown in figures 1.34 and 1.35, where the measurements in [9] are shown for comparison. Good agreement is found in both cases, and the efficiency variations are of the order of 15% over the camera surface. The result of 0.85 for the lowest value of the efficiency obtained in the measurements is thus reproduced by the simulation. The steep fall in the extremes of the scan in the laboratory data is due to the fact that in the laboratory
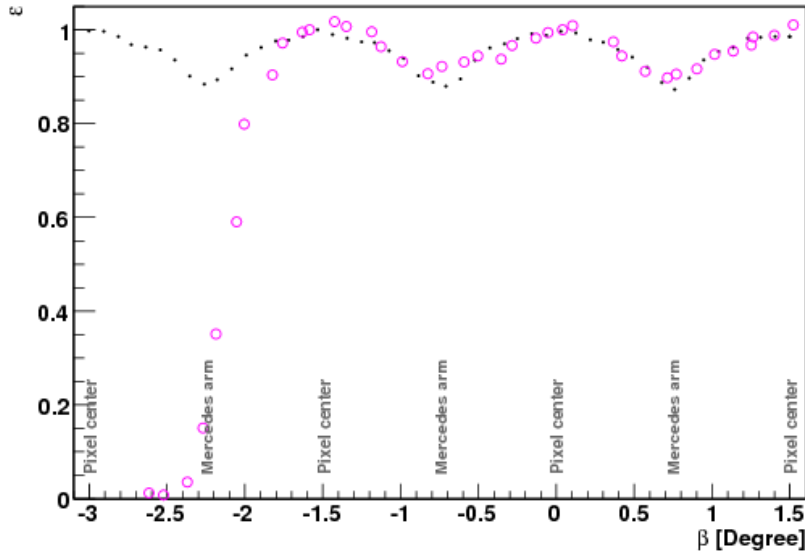
Figure 1.35: Relative efficiency along a horizontal line passing through pixel centres. The black dots are the simulation results and the white circles are the measurements from [9].

1 setup only 7 pixels were present.

1.4.2   Comparison with Laser Events

3 The Central Laser Facility (CLF)[10], placed within the array at a position equidis-
4 tant from the Los Leones, Los Morados and Coihueco FDs, fires 355 nm vertical or
5 inclined laser pulses with an energy of 8 mJ. The light from the laser beam is dif-
6 fused in the atmosphere and detected by the FDs. As the light from the laser beam
7 travels upwards in the atmosphere it is isotropically diffused. Some of this diffuse
8 light is emitted towards the Fluorescence Telescopes. The light propagates through
9 the atmosphere for around 30 km suffering attenuation until it reaches the detector.
10 At each moment in time the CLF can be considered as a point source, producing a
11 spot in the focal surface dominated by the optical properties of the telescope.

12   In figure 1.36 the track of a vertical laser shot in the FD camera is shown in
13 (α, β) coordinates along with a zoom of the region of interest. The corresponding
14 measured light profile (number of photons as a function of time) is shown in 1.37 .
15 This typical profile is the convolution of the attenuation and scattering of the up-
16 going laser beam with the attenuation of the light from the laser to the fluorescence
17 telescope and the non-uniformities of the FD camera. Here we are interested in
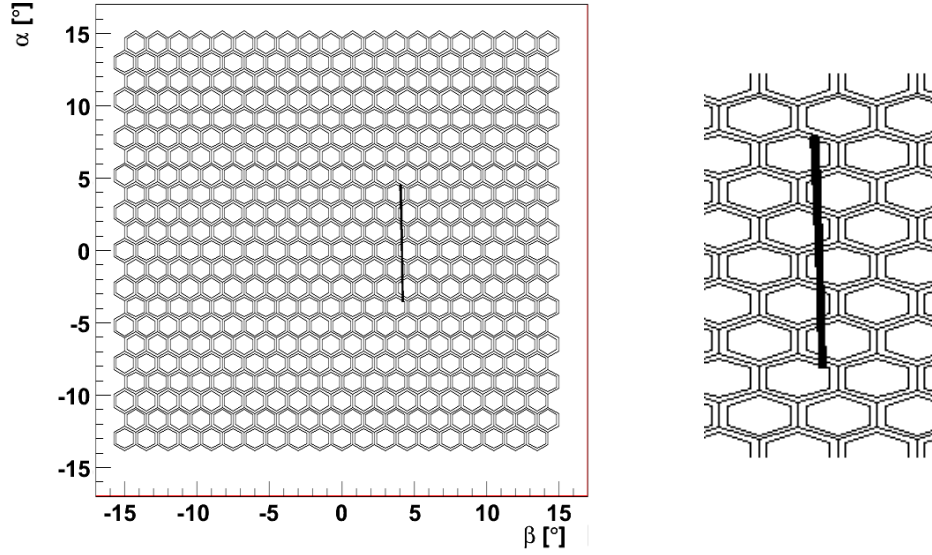18 isolating this last effect. In this study, the lower part of the shower track was

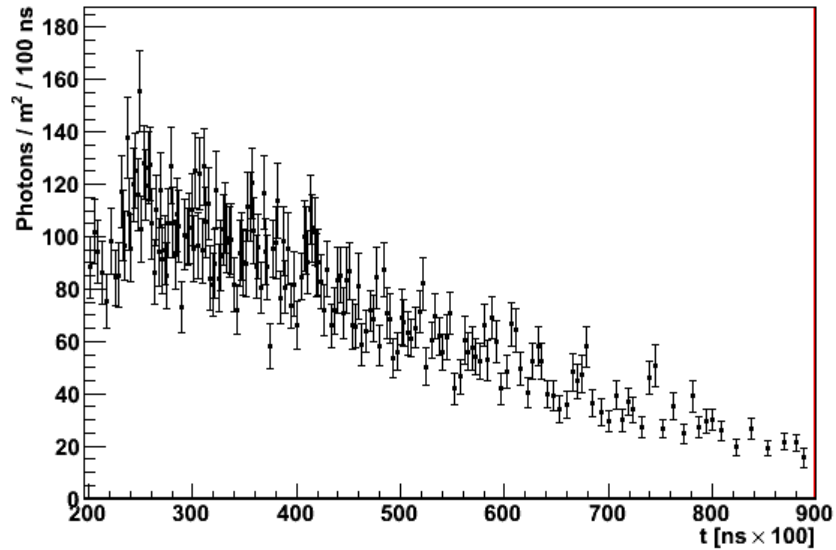Figure 1.36: Track of a vertical laser shot. A zoom is presented in the image on the right.

Figure 1.37:   The laser light profile.

1 discarded to avoid the region in which Mie scattering cannot be neglected. In the
2 same way, the upper part of the shower track was discarded to avoid the timeslots
3 with low statistics.

4   The expected number of photons arriving at the telescope diaphragm, N_γ^{lens}, with
5 a direction falling within a given (α, β) bin can be parametrised as:

$$N_\gamma^{\text{lens}} = I_0 \times exp\left(-\frac{d_1}{d_0}\right) \times dir(h) \times \Delta\Omega(h) \times exp\left(-\frac{d_2}{d_0}\right)$$

6 where I_0 is the laser intensity, the first exponential term describes the attenuation of
7 the upgoing laser beam in terms of the atmosphere traversed d_1, the function $dir(h)$
8 describes the beam scattering at the height h, $\Delta\Omega(h)$ is the solid angle subtended
9 by the telescope aperture at a given point of the laser beam and the second expo-
10 nential term describes the attenuation of scattered photons when they traverse an
11 atmospheric depth of d_2 in its propagation from the scattering point in the beam to
12 the eye. In fact, $dir(h)$ describes the direction dependence of Rayleigh scattering (in
13 other words its differential cross-section) and is well described by a second degree
14 polynomial:

$$dir(h) = a_0 + a_1 cos\theta_z + a_2 cos\theta_z^2$$

15 where θ_z is the photon scattering direction with respect to the direction of the up
16 going laser beam.

17   The number of photons expected in the camera, N_γ^{camera}, in the same (α, β) bin
18 is given by

$$N_\gamma^{\text{camera}} = N_\gamma^{\text{lens}} \cdot \varepsilon_{\text{telescope}}$$

19 where $\varepsilon_{\text{telescope}}$ is the telescope efficiency and can be expressed as

$$\varepsilon_{\text{telescope}} = \varepsilon_{\text{mean}} \cdot \varepsilon_{\text{relative}}$$

20 where $\varepsilon_{\text{mean}}$ is the average efficiency of the telescope and $\varepsilon_{\text{relative}}$ contains the ef-
21 ficiency variations along the camera. This relative efficiency is thus given by the
22 ratio between the number of detected photons, N_γ, and the average expected signal,
23 $\overline{N_\gamma^{\text{camera}}} = N_\gamma^{\text{lens}} \cdot \varepsilon_{\text{mean}}$.

24   Taking into account that the constant terms like I_o and $\varepsilon_{\text{mean}}$ can be absorbed
25 by the free parameters, that there is a one-to-one transformation between the laser
26 curve camera coordinates (α, β) and the time slot and assuming that the atmospheric
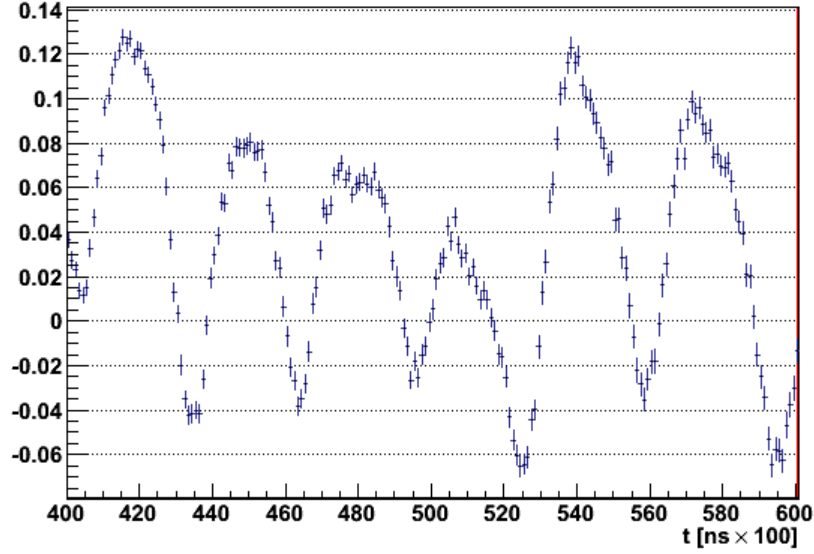27 density varies with the height h as $\rho(h) \propto e^{-h/L}$, the average number of photons in

Figure 1.38: Relative differences of the fitted and measured number of photons. The average over one month of laser data is shown.

each time bin can be expressed as

$$\overline{N_\gamma^{\mathrm{camera}}}(t) = \frac{2c^2t^2}{c^4t^4 + l^4} \cdot \left(\frac{P_3}{t^2} + P_2 \cdot t + P_1\right) \times$$
$$\exp\left\{\left[\frac{-1}{L}\left(\frac{c^2t^2 - l^2}{2ct} - \left(\frac{c^2t^2 - l^2}{2ct}\right)^2 + \left(\frac{c^2t^2 - l^2}{2ct}\right)^3\right)\right]\frac{1}{2(c^2t^2 - l^2)}\right\}$$

where c is the speed of light, l is the distance from the laser to the fluorescence telescope and P_1, P_2, P_3 and L are free parameters. These free parameters are fixed fitting this formula to the laser light profile.

The relative differences between the fitted value and the measured number of photons (N_γ), given by

$$\frac{N_\gamma - \overline{N_\gamma^{\mathrm{camera}}}}{\overline{N_\gamma^{\mathrm{camera}}}}$$

are shown in figure 1.38. In the figure the data result from the average of the laser data available in one month. The distribution of the values in the figure have a mean value of 0.03. The same analysis for other months shows that the mean value is stable and varies between 0.03 and 0.04. The non-existence of a trend in these data indicate that the method used to extract the relative efficiencies is reliable and stable.

In figure 1.39 the relative efficiencies $\varepsilon_{\mathrm{relative}} = \frac{N_\gamma}{N_\gamma^{\mathrm{camera}}}$ for 18 months of laser data
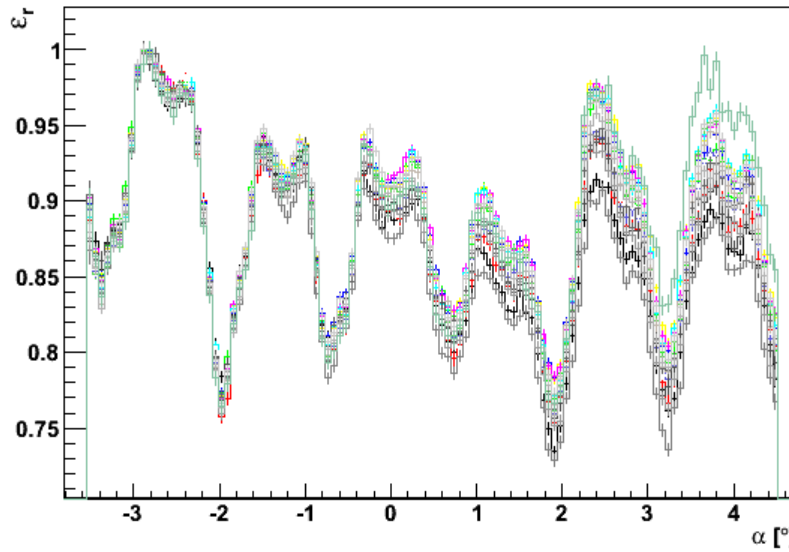
Figure 1.39: Relative efficiency across the FD camera for 18 months of CLF laser shots.

are shown. The values obtained were rescaled setting the maximum to 1. In this figure the reduction in the efficiency due to the Mercedes is clearly visible. It is also clear that the relative efficiency is quite stable over this 18 month period. It can also be seen that there are variations in the maximum and minimum efficiencies from pixel to pixel which is unexpected if all the pixels were equivalent.

In figure 1.40 the relative efficiency estimated with laser data is compared to the one obtained with the $\overline{\text{Off}}$ $\underline{\text{line}}$ standard laser simulation. While the overall shapes agree, there are some differences between the simulation and the data. In particular, the data show deeper valleys than the simulation and do not reproduce some features that seem to be related to individual pixels.

The variations from pixel to pixel can be smoothed out by folding the laser data into a virtual pixel. In this virtual pixel a vertical laser shot actually scans two different regions of the pixel in β. The virtual pixel with the positions scanned by the laser track is shown in figure 1.41. To better evaluate the efficiency drop between the central region of the pixel and the peripheral region, six regions were defined in the virtual pixel, as shown in figure 1.42. Regions 1 and 2 are defined near the centre of the pixel and should be the areas of the pixel with higher efficiency, while regions 3, 4, 5 and 6 are defined in the Mercedes area and should present a reduced efficiency, due to the Mercedes inefficiency. The efficiency for all the points that fall inside each region was averaged and the results are shown in figure 1.43. The ratio
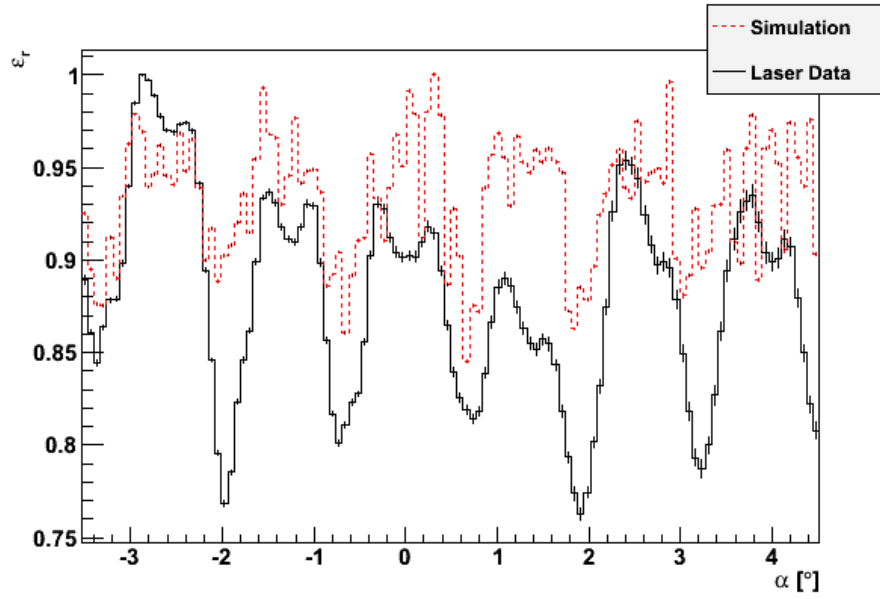
Figure 1.40: The relative efficiency across the FD camera measured from CLF laser shots (solid black line) and obtained with the standard $\overline{\text{Off}}$ $\underline{\text{line}}$ simulation (dashed red line).
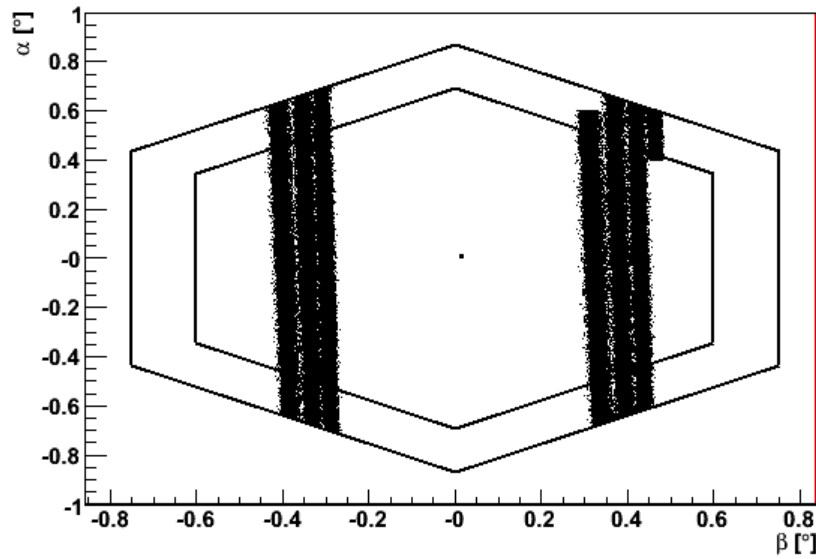

Figure 1.41: The virtual pixel with the folded laser track represented.
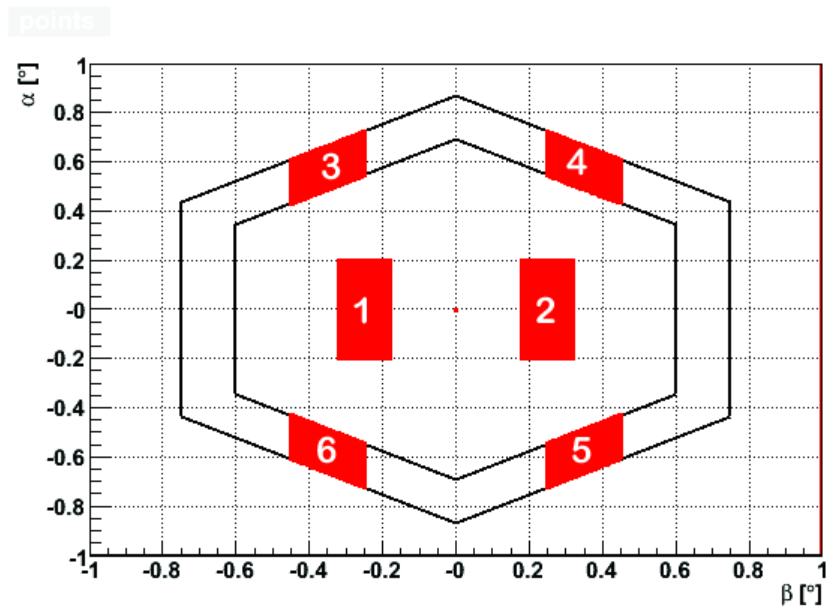
Figure 1.42: The six regions defined on the virtual pixel for the calculation of the R parameter.
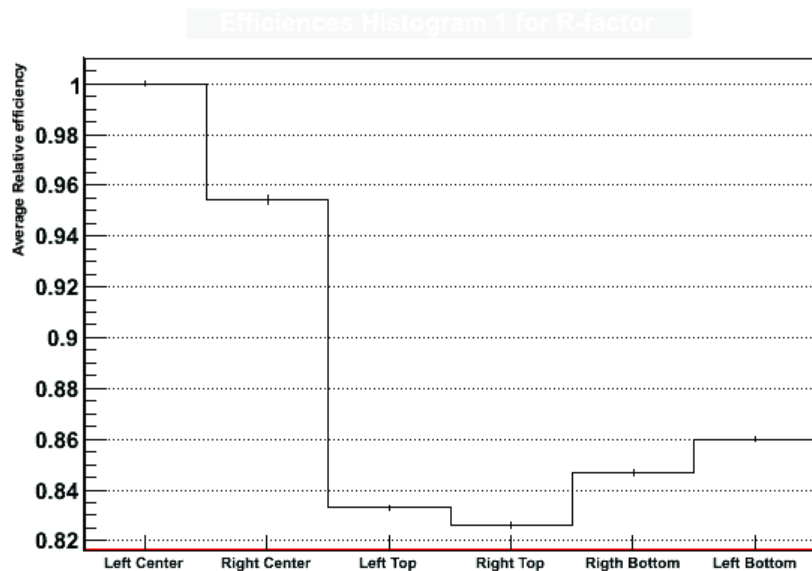

Figure 1.43: Relative efficiency for the six zones defined in the virtual pixel.
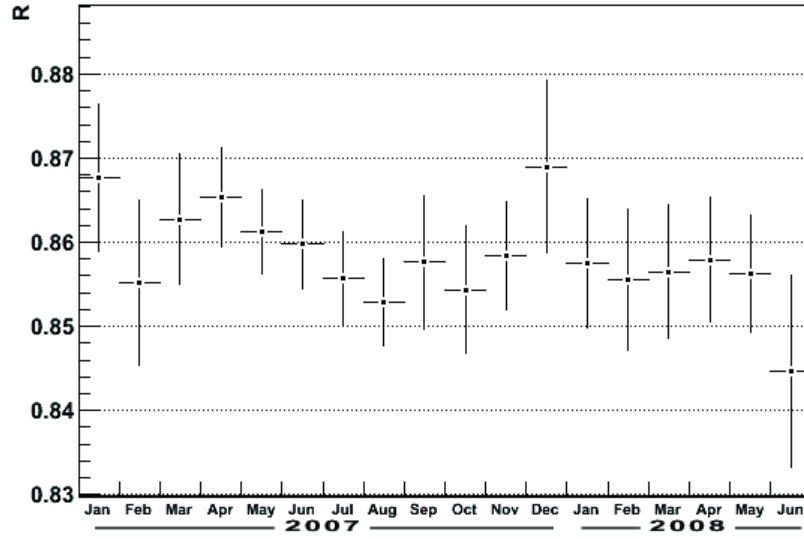
Figure 1.44: Evolution of the R parameter, obtained from laser data, with time.

R between the average efficiency in the peripheral regions and the average efficiency in the central regions measures the efficiency drop due to the Mercedes and amounts to $R = 0.858 \pm 0.008$. In figure 1.44 the evolution of the R parameter with time for an 18 month period is shown. It can be seen that this parameter is, within errors, stable over time.

The R parameter was also evaluated using the TelescopeSimulatorLX, and the value obtained, $R = 0.937 \pm 0002$, is not compatible with the result obtained from laser data. This difference may be related to a bad description of the optical spot and/or to the Mercedes efficiency in the simulation. A first study of the influence of the Mercedes reflectivity and of the spot size was performed using the Geant4 simulation. Two different configurations were tested and scans were performed in the central pixel of the laser track.

In the first configuration the Mercedes surface reflectivity in the simulation was reduced from the nominal value of 0.90 to 0.85 and to the limit value of 0. In figure 1.45 the relative efficiency is shown versus the angle α in the central region of the camera for the laser data and for the Geant4 simulation with a Mercedes reflectivity of 0.85 and 0. In the right image the data have been rescaled setting the maximum to 1. If the spot was very small, a reduction on the Mercedes efficiency should only affect the region of the scan on top of the Mercedes (around $\alpha \sim 0.7°$). Namely, when the reflectivity was set to 0 the efficiency in this region should also drop to 0 as no photons would be reflected. However, from the left figure it is clear that
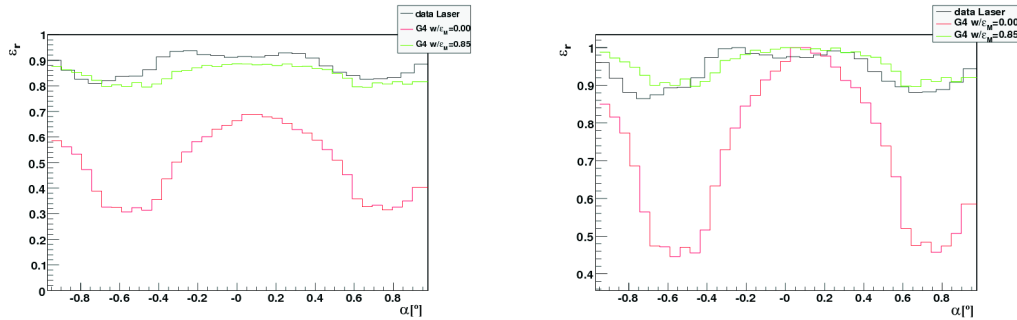
Figure 1.45: Profiles of the relative efficiency versus the angle α in the central region of the camera. Data is represented in black. In green and red are represented the simulations with a Mercedes reflectivity of 0.85 and 0, respectively. The data on the right image has been rescaled setting the maximum to 1.

the efficiency drop is lower than expected. Moreover the reduction in the Mercedes efficiency affects also the central region. This indicates that the spot, along the incident directions, is such that there is a reflected component when photons are directed to the pixel centre and that there exists a direct component when the photons are directed to the Mercedes. Thus, changing the Mercedes reflectivity the simulation can reproduce the deeper valleys seen in the data but affects also the whole profile shape making a smoother transition.

To test the influence of the spot size in the relative efficiency, the flexibility of the TelescopeSimulatorLX was used to reduce, in an effective way, the optical spot size. This reduction was achieved by rescaling the positions and incidence angles of the photons in the focal surface. Two scans were performed with scale factors of 100% and 10%, representing two limit cases, and two scans with intermediate scan factors of 70% and 50%. The relative efficiencies for the four scans are shown in figure 1.46 . The scan with a 10% scaling factor puts in evidence the reduction in the efficiency in the Mercedes areas, due to the reduction of the direct component, and the increase of the relative efficiency in the central regions as the component reflected in the Mercedes is reduced. It can also be seen that the profiles get steeper with the reduction of the spot size.

Neither of these effects can, by itself, correct the disagreement between data and simulation. A more systematic study will be therefore needed. This study should include laser data from the several fluorescence eyes and, if possible, shower events data.
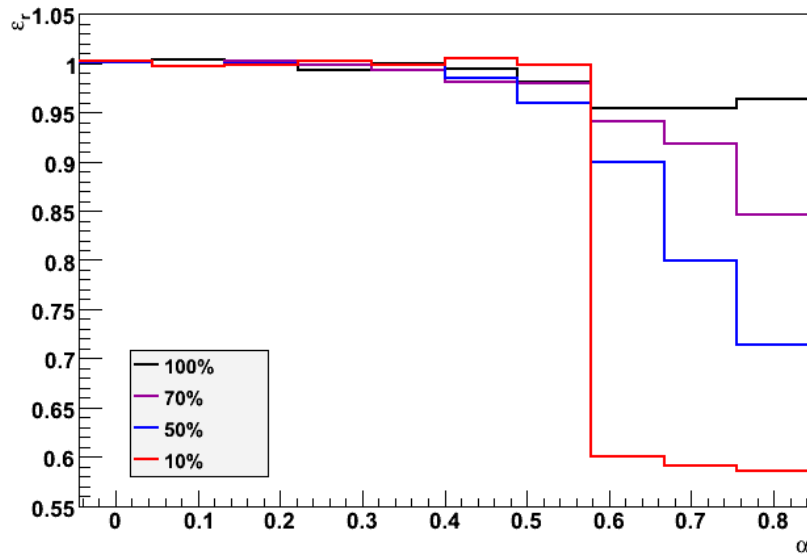
Figure 1.46: Profiles of the relative efficiency versus the angle α in the central region of the camera for several spot sizes. The four profiles were made with scaling factors of 100%, 70%, 50% and 10% are represented with different colours that are indicated in the legend.

Bibliography

[1] M. Born and E. Wolf. *Principles of Optics*. Cambridge Univ. Press, 1999.

[2] Special filter glasses for sun beds, advanced materials, schott, March 2006.

[3] M.A.L. de Oliveira, V. de Souza, H.C. Reis, and R. Sato. Manufacturing the Schmidt corrector lens for the Pierre Auger Observatory. *Nuclear Instruments & Methods in Physics Research Section A-Accelerators Spectrometers Detectors and Associated Equipment*, 522:360–370, 2004.

[4] R. Sato. *Desenvolvimento e produção das lentes dos telescópios do Observatorio Auger*. PhD thesis, Universidade Estadual de Campinas. Instituto de Física 'Gleg Wataghin', 2005.

[5] C. Aramo, R. Fonte, D. Nicotra, G. Gallo, G. Raia, F. Bracci, P. Facal, G. Matthiae, P. Privitera, and G. Vitali. The camera of the auger fluorescence detector. Technical Report GAP-99-027, Pierre Auger Observatory, 1999.

[6] S. Argirò, S.L.C. Barroso, J. Gonzalez, L. Nellen, T. Paul, T.A. Porter, L. Prado Jr., M. Roth, R. Ulrich, and D. Veberič. The offline software framework of the pierre auger observatory. *Nucl. Instrum. Meth. A*, 580:1485–1496, 2007.

[7] J. Allison, K. Amako, J. Apostolakis, H. Araujo, P. A. Dubois, M. Asai, G. Barrand, R. Capra, S. Chauvie, R. Chytracek, G. A. P. Cirrone, G. Cooperman, G. Cosmo, G. Cuttone, G. G. Daquino, M. Donszelmann, M. Dressel, G. Folger, F. Foppiano, J. Generowicz, V. Grichine, S. Guatelli, P. Gumplinger, A. Heikkinen, I. Hrivnacova, A. Howard, S. Incerti, V. Ivanchenko, T. Johnson, F. Jones, T. Koi, R. Kokoulin, M. Kossov, H. Kurashige, V. Lara, S. Larsson, F. Lei, O. Link, F. Longo, M. Maire, A. Mantero, B. Mascialino, I. McLaren, P. M. Lorenzo, K. Minamimoto, K. Murakami, P. Nieminen, L. Pandola, S. Parlati, L. Peralta, J. Perl, A. Pfeiffer, M. G. Pia, A. Ribon, P. Rodrigues, G. Russo, S. Sadilov, G. Santin, T. Sasaki, D. Smith, N. Starkov, S. Tanaka, E. Tcherniaev, B. Tome, A. Trindade, P. Truscott, L. Urban, M. Verderi, A. Walkden,

J. P. Wellisch, D. C. Williams, D. Wright, and H. Yoshida. Geant4 developments and applications. *IEEE Transactions on Nuclear Science*, 53(1):270–278, 2006.

[8] S. Agostinelli, J. Allison, K. Amako, J. Apostolakis, H. Araujo, P. Arce, M. Asai, D. Axen, S. Banerjee, G. Barrand, F. Behner, L. Bellagamba, J. Boudreau, L. Broglia, A. Brunengo, H. Burkhardt, S. Chauvie, J. Chuma, R. Chytracek, G. Cooperman, G. Cosmo, P. Degtyarenko, A. Dell'Acqua, G. Depaola, D. Dietrich, R. Enami, A. Feliciello, C. Ferguson, H. Fesefeldt, G. Folger, F. Foppiano, A. Forti, S. Garelli, S. Giani, R. Giannitrapani, D. Gibin, J. J. G. Cadenas, I. Gonzalez, G. G. Abril, G. Greeniaus, W. Greiner, V. Grichine, A. Grossheim, S. Guatelli, P. Gumplinger, R. Hamatsu, K. Hashimoto, H. Hasui, A. Heikkinen, A. Howard, V. Ivanchenko, A. Johnson, F. W. Jones, J. Kallenbach, N. Kanaya, M. Kawabata, Y. Kawabata, M. Kawaguti, S. Kelner, P. Kent, A. Kimura, T. Kodama, R. Kokoulin, M. Kossov, H. Kurashige, E. Lamanna, T. Lampen, V. Lara, V. Lefebure, F. Lei, M. Liendl, W. Lockman, F. Longo, S. Magni, M. Maire, E. Medernach, K. Minamimoto, P. M. de Freitas, Y. Morita, K. Murakami, M. Nagamatu, R. Nartallo, P. Nieminen, T. Nishimura, K. Ohtsubo, M. Okamura, S. O'Neale, Y. Oohata, K. Paech, J. Perl, A. Pfeiffer, M. G. Pia, F. Ranjard, A. Rybin, S. Sadilov, E. Di Salvo, G. Santin, T. Sasaki, N. Savvas, Y. Sawada, et al. Geant4-a simulation toolkit. *Nuclear Instruments & Methods in Physics Research Section A-Accelerators Spectrometers Detectors and Associated Equipment*, 506(3):250–303, 2003.

[9] P. Facal San-Luis and P. Privitera. Measurement of the FD camera light collection effciency and uniformity. Technical Report GAP-2000-010, Pierre Auger Observatory, 2000.

[10] Brian Fick, James Matthews, John Matthews, Rishi Meyhandan, Megan McEwen, Miguel Mostafá, Michael Roberts, Paul Sommers, and Lawrence Wiencke. The first central laser facility. Technical Report GAP-2004-003, Pierre Auger Observatory, 2003.